MiR-155 epigenetically counteracts hypoxia for mitochondrial fitness during germinal center positive selection

Rinako Nakagawa[1*], Miriam Llorian[2], Sunita Varsani-Brown[3], Probir Chakravarty[2], Jeannie M. Camarillo[4], David Barry[5], Roger George[6], Neil P. Blackledge[7], Graham Duddy[3], Neil L. Kelleher[4], Robert J. Klose[7], Martin Turner[8] and Dinis P. Calado[1*]

1. Immunity and Cancer Laboratory, Francis Crick Institute, London, UK.
2. Bioinformatics and Biostatistics Laboratory, Francis Crick Institute, London, UK.
3. Genetic Modification Service Laboratory, Francis Crick Institute, London, UK.
4. Department of Chemistry, Molecular Biosciences and the National Resource for Translational and Developmental Proteomics, Northwestern University, Evanston, IL, USA.
5. Advanced Light Microscopy Laboratory, Francis Crick Institute, London, UK.
6. Structural Biology Laboratory, Francis Crick Institute, London, UK.
7. Department of Biochemistry, University of Oxford, Oxford, UK.
8. Immunology Programme, The Babraham Institute, Cambridge, UK.

* To whom correspondence may be addressed. Email: rinako.nakagawa@crick.ac.uk or dinis.calado@crick.ac.uk.

Key words
Mir155, germinal center B cells, positive selection, mitochondria, OXPHOS, ROS, hypoxia, epigenetic regulation, H3K36me2, *Kdm2a*.

Abstract

Germinal center (GC)-B cell proliferation relies on oxidative phosphorylation. Positively selected GC-B cells initiate cell division in the hypoxic light zone (LZ) microenvironment and continue vigorous proliferation upon migration to the dark zone. However, the mechanisms underlying how these GC-B cells reprogram mitochondrial bioenergetic functions to sustain cell division while overcoming hypoxia-driven energy stress are not understood. We found that microRNA (miR)-155 directly repressed the expression of hypoxia-induced histone lysine demethylase 2a, resulting in fine-tuning of histone H3 di-methylated lysine 36 levels. This regulation optimized the expression of vital nuclear mitochondrial genes in LZ GC-B cells, thereby preventing excessive production of mitochondrial reactive oxygen species and apoptosis. Thus, miR-155-regulated epigenetic mechanisms facilitate dynamic mitochondrial remodeling of LZ GC-B cells.

Introduction

Germinal centers (GCs) transiently form in B cell follicles of secondary lymphoid organs upon infection or vaccination. GCs are indispensable sites for increasing the affinity of antibodies, i.e., for the production of high-affinity antibody-secreting plasma cells that are critical for protecting hosts from pathogens. The process by which antibodies increase affinity to the antigen is called affinity maturation (*1, 2*) and occurs in GCs through a bidirectional migration cycle between two regions, the light zone (LZ) and the dark zone (DZ) (*3*). In the LZ, GC-B cells undergo antigen-driven selection in response to signals from B cell receptor (BCR) engagement and T follicular helper cells (TFHs) (*4*). Positively selected LZ GC-B cells induce *Myc*, a critical cell cycle regulator required for GC maintenance, and the transient c-MYC expression marks "licensed" GC-B cells (*5, 6*). Following positive selection signals, GC-B cells initiate cell division in the LZ and vigorously proliferate after their transit to the DZ (*7*).

Mitochondrial oxidative phosphorylation (OXPHOS) is essential for GC-B cells to proliferate in the DZ (*8, 9*). In contrast, quiescent GC-B cells seem to depend on glycolysis (*10*). This is concordant with recent reports showing that the LZ, where predominantly quiescent cells reside, represents a hypoxic microenvironment (*10-12*). Hypoxia promotes glycolysis (*13*) and suppresses energy consuming processes, such as cell cycle progression and translation (*14-16*). Therefore, cells under hypoxic conditions generally arrest the cell cycle. During positive selection, however, GC-B cells substantially change gene expression profiles to ensure their survival and proliferation in the LZ before migrating to the DZ (*4, 7, 17-19*). To trigger transcriptional changes coupled with cell division in the LZ, cMyc$^+$ GC-B cells must overcome hypoxia-induced energy stress through metabolic fine-tuning. However, the mechanism by which metabolic profiles are regulated in LZ GC-B cells during positive selection remain unknown.

Here, we found that microRNA (miR)-155 is essential to remodel mitochondria, thus altering mitochondrial bioenergetic functions of cMyc$^+$ LZ GC-B cells by counteracting hypoxia-driven effects. In cMyc$^+$ LZ GC-B cells, miR-155 directly repressed the expression of hypoxia-induced histone lysine demethylase 2a (*Kdm2a*). *Kdm2a* is associated with the inactivation of gene transcription through its preferential demethylation of di-methylated lysine 36 of histone H3 (H3K36me2). The resultant histone modifications variably regulate cell proliferation depending on the genes it targets (*20-23*). MiR-155-mediated repression of *Kdm2a* in cMyc$^+$ LZ GC-B cells enabled fine-tuning of H3K36me2 levels at promoters and transcription start sites (TSSs), and subsequently facilitated optimal expression of key nuclear mitochondrial genes. These epigenetic modifications allowed metabolic adaptation of GC-B cells to overcome hypoxia in the LZ microenvironment. This adaptation enabled GC-B cells to generate energy through OXPHOS and to support vigorous proliferation in the DZ. In the absence of miR-155, mitochondria in cMyc$^+$ LZ GC-B cells became dysfunctional, causing exacerbated oxidative stress and subsequent cell death, particularly in the DZ. Hence, miR-155 counteracts hypoxia-driven effects by modulating the epigenetic network of LZ GC-B cells during positive selection to activate mitochondrial bioenergetic functions for their proliferation.

Results

Mitochondrial ROS production is exacerbated by Mir155-deficiency in GC-B cells.

OXPHOS is required to support the robust proliferation of GC-B cells with high affinity BCRs in the DZ (*9*). Mitochondrial reactive oxygen species (ROS) are produced during normal OXPHOS activity at the electron transport chain on the inner mitochondrial membrane (*24*). However, defective mitochondria drive overproduction of ROS, which can activate apoptotic pathways (*25*). MiR-155 is predominantly expressed in cMyc$^+$ GC-B cells and is known to protect cMyc$^+$ GC-B cells from apoptosis, particularly those with high affinity BCRs (*26*). Therefore, we hypothesized that miR-155 prevents cell death, in part, by limiting excessive production of mitochondrial ROS.

To test the hypothesis, we utilized the SW_{HEL} adoptive transfer system which allowed us to investigate miR-155 functions in GC-B cells in a B cell-intrinsic manner. In this system, B cells from *Mir155*-sufficient or *Mir155*-deficient SW_{HEL} *Myc$^{gfp/gfp}$ Aicda-cre*-h*CD2* mice were transferred into CD45.1$^+$ congenic recipient mice. SW_{HEL} mice express the hen egg lysozyme (HEL)-specific immunoglobulin heavy chain knock-in and light chain transgene (HyHEL10 BCR) (*27*). *Myc$^{gfp/gfp}$* reporter mice express a GFP-cMYC fusion protein from the endogenous *Myc* locus (*28*). *Aicda-cre*-h*CD2* transgenic mice carry a *Cre* gene linked with a truncated human *CD2* cDNA via an internal ribosome entry site (IRES) under the control of *Aicda* promoter (*29*). In these mice, positively selected cMyc$^+$ GC-B cells were identified by GFP fluorescence and hCD2 surface expression. Recipient mice that received transferred B cells were challenged with HEL3$^\times$ (**Fig.1A**). Donor GC-B cells (CD45.1$^-$ CD45.2$^+$ B220$^+$ hCD2$^+$ CD38^{lo} CD95$^+$) were gated as described in ***Supplemental Figure 1A***, and by coupling DZ/LZ distinguishing markers (CXCR4/CD86) to cMyc-GFP expression. Then, GC-B cells were subdivided into four consecutive subpopulations: cMyc$^-$ LZ, cMyc$^+$ LZ, cMyc$^-$ DZ and cMyc$^+$ DZ (*7*). MiR-155 is mostly co-expressed with cMyc in GC-B cells, and the expression of both cMyc and miR-155 changes as follows: highest levels in cMyc$^+$ LZ GC-B cells, intermediate levels in cMyc$^+$ DZ GC-B cells and followed by negligible levels in cMyc$^-$ DZ and cMyc$^-$ LZ GC-B cells (*5, 6, 26*) (***Supplemental Figure 1B***). Lack of miR-155 did not impact the expression of cMyc in GC-B cells, hence the mean fluorescent intensity (MFI) of cMyc-GFP was comparable between wildtype (hereafter called as "WT") and *Mir155*-knock out (hereafter called as "KO") cells (***Supplemental Figure 1C***). However, the number of cMyc$^+$ LZ and cMyc$^+$ DZ GC-B cells were significantly reduced in the absence of miR-155 (***Supplemental Figure 1D***). The MitoSOX-based flow cytometric assay for the detection of mitochondrial ROS revealed that in the absence of miR-155, GC-B cell subpopulations, including cMyc$^+$ LZ, cMyc$^+$ DZ and cMyc$^-$ DZ, exhibited a significantly higher percentage of MitoSOX$^+$ cells compared to their respective WT cells (**Fig.1B**). Additionally, we observed a concurrent increase in the proportion of active-caspase 3$^+$ cells within the cMyc$^+$ LZ, cMyc$^+$ DZ and cMyc$^-$ DZ subpopulations of the KO mice compared to the WT mice (**Fig. 1B**). These findings indicate that miR-155 plays a role in mitigating mitochondrial ROS levels in GC-B cells.

MiR-155 is required for promoting mitochondrial fitness in GC-B cells.

To gain a comprehensive understanding of miR-155-mediated regulation of mitochondrial functions and dynamics of OXPHOS activity during the migration cycle of GC-B cells, we conducted single cell (sc) RNA-seq on both WT and KO GC-B cells and dissected GC-B cells into distinct subpopulations. Unsupervised clustering identified nine distinct clusters: LZ signature genes (*9*) were expressed in clusters 0, 1, 2, 5 and 8, and clusters 0 and 1 predominantly represented cMyc$^-$ LZ GC-B cells due to their enrichment in the G1 phase of the cell cycle (***Supplemental Figure 1E*** to ***1G***). Cluster 8 showed enrichment in pre-memory B cell (pre-MBC)-associated genes, such as *Ccr6*, *Cd38* and *Hhex* (*30, 31*)), indicating its representation of pre-MBC cells (***Supplemental Table 1***). DZ signature genes (*9*) were expressed in clusters 3, 4, 5, 6 and 7 (***Supplemental Figure 1G***), which correlated strongly with cell cycle progression, i.e., cluster 6; S phase, cluster 4; S→G2/M phase, cluster 7; G2/M phase and cluster 3; G2/M→G1 phase (***Supplemental Figure 1E***). The order of the clusters likely reflects a temporal sequence of DZ GC-B cells as clusters 6 → 4 → 7 → 3.

To establish more specific relationships between the clusters we employed partition-based graph abstraction (PAGA) (*32*). The PAGA graph revealed that LZ clusters 0, 1, 2 and 8 formed a closely interconnected group, while DZ clusters 3, 4, 6 and 7, characterized by high expression of *Cxcr4*, formed a distinct group (**Fig.1C** and ***Supplemental Figure 1H***). Cluster 5, which exhibited higher mitochondrial content but lower gene counts than the other clusters, did not belong to either LZ or DZ groups (**Fig.1C** and ***Supplemental Figure 1H*** and ***1I***). Notably, this cluster displayed a significant decrease in rRNA levels (***Supplemental Figure 1J***), which is indicative of early apoptosis (*33*). Therefore, we excluded cluster 5 from further analysis. The high expression of *Myc* in clusters 2 (LZ) and 6 (DZ) in the PAGA graph corresponded to the enrichment of *Myc* signature genes (*5, 6*) observed in these clusters, as shown in the UMAP (**Fig.1C** and ***Supplemental Figure 1G***). The increased *Myc* expression in cluster 8 (pre-MBCs) in **Fig.1C** is consistent with our previous work suggesting that cMyc-induced positively selected GC-B cells can give rise to MBCs (*7, 34*). In the PAGA graph, clusters 0 (LZ) and 3 (DZ) predominantly connect the LZ and DZ groups (**Fig.1C** and ***Supplemental Figure 1H***), indicating that cluster 0 represents LZ B cells soon after migration back from the DZ. The temporal and spatial dynamics of the clusters are summarized in **Fig.1D**.

Using these temporally linked GC-B cell clusters, we investigated the changes in mitochondrial functions in GC-B cells in the absence of miR-155 by calculating the gene signature scores for "mitochondrion" and "OXPHOS". We found these to be significantly lower in cluster 2 (cluster enriched with cMyc$^+$ LZ GC-B cells) and all the DZ clusters (clusters 6, 4, 7 and 3) of KO cells than those of WT cells (**Fig.1E**). These results suggest that the absence of miR-155 led to impaired mitochondrial functions in cMyc$^+$ LZ GC-B cells (cluster 2) and cMyc$^+$ DZ GC-B cells (cluster 6), and that such impairment was still observed in cMyc$^-$ DZ GC-B cells (clusters 4, 7 and 3) that no longer express miR-155 in WT mice. Thus, miR-155 plays a critical role in maintaining mitochondrial integrity in cMyc$^+$ GC-B cells and likely impacts the bioenergetic functions in GC-B cells.

To further clarify the regulatory role of miR-155 in LZ GC-B cells, we carried out bulk RNA-seq analysis on WT and KO cMyc$^+$ LZ GC-B cells. Gene set enrichment analysis (GSEA) on RNA-seq data revealed the top eight enriched biological pathways in WT cMyc$^+$ LZ GC-B cells compared to KO cMyc$^+$ LZ GC-B cells were related to "ribosome", "translation" and "mitochondria", either alone or in combination (***Supplemental Figure 1K***). Nearly half of the significantly increased genes in the top three pathways ("ribosomal subunit", "Structural constituent of ribosome" and "ribosome") encoded mitochondrial ribosomal proteins (***Supplemental Table 2***). Mitochondrial ribosomal proteins are encoded by nuclear genes and are subsequently transported to the mitochondria following their synthesis in the cytoplasm (*35*). The Cytoscape network analysis of GSEA results revealed an enrichment of pathways involved in mitochondrial protein transport and mitochondrial functions, particularly electron transport, in WT cMyc$^+$ LZ GC-B cells compared to their KO counterparts (**Fig.1F)**. This finding indicates that these pathways are compromised or defective in KO cMyc$^+$ LZ GC-B cells. In line with the enrichment map, genes associated with "OXPHOS", and "Mitochondrial translation" exhibited a significant enrichment in WT cMyc$^+$ LZ GC-B cells compared to KO cMyc$^+$ LZ GC-B cells, suggesting impaired functionality of these pathways in KO cMyc$^+$ LZ GC-B cells (**Fig.1F)**. Collectively, our findings suggest that mitochondrial fitness is exclusively established in the LZ during positive selection and that miR-155 expressed in the LZ is critical for maintaining mitochondrial bioenergetic functions in GC-B cells.

MiR-155 regulates H3K36me2 levels in dividing LZ GC-B cells.

To visualize the enriched pathways in KO cells, we generated a Cytoscape enrichment map using RNA-seq data from cMyc$^+$ LZ GC-B cells. The enrichment map revealed that the gene signature "Demethylation" was the only pathway significantly enriched in KO cMyc$^+$ LZ GC-B cells when compared to WT cells (**Fig. 2A**). The signature "Demethylation" consisted of four pathways: "Histone demethylase activity", "Protein demethylation", "Demethylase activity", and "Demethylation" (**Fig. 2A**). Therefore, we investigated whether there were any alterations in histone post-translational modifications (PTMs) in KO GC-B cells compared to WT GC-B cells. To this end, we employed a liquid chromatography with tandem mass spectrometry (LC-MS/MS) technique that allows unbiased identification and quantitative profiling of histone PTMs (*36, 37*). This method successfully quantified the abundance of histone PTMs in both WT and KO LZ GC-B cells, including methylation and acetylation on histone H1.4, H3 and H4. The analysis showed a significant decrease in di-methylation of histone H3.1 at lysine 36 (K36me2) and an increase in unmethylated histone H3 at lysine 23 (K23me0) in KO LZ GC-B cells compared to WT LZ GC-B cells (**Fig.2B** and ***Supplemental Figure 2A***). We also observed a decrease in acetylation of H3 at K23 (K23ac) (***Supplemental Figure 2A***), which is linked to transcriptional activation (*38*). Acetylation of H3 at K23 can be catalyzed by cyclic adenosine monophosphate response element binding protein binding protein (CREBBP), monocytic leukemia zinc finger protein (MOZ) complex and its paralog monocytic leukemia zinc finger related factor (MORF) complex (*38, 39*). However, there were no differentially expressed genes (DEGs) in the bulk RNA-seq dataset

between KO and WT cMyc$^+$ LZ-GC-B cells for any genes encoding protein products that are part of these complexes (***Supplemental Table 2***). Therefore, it was unlikely that the absence of miR-155 was directly responsible for the decreased H3K23ac levels in KO LZ GC-B cells. Because the reduction of H3K23ac could lead to increased levels of unmethylated H3K23, the elevation in H3K23me0 levels appears to be not directly caused by the lack of miR-155 either. Thus, the decreased levels of K36me2 on histone H3.1 appeared to be the sole altered histone methylation directly impacted by the absence of miR-155-mediated regulation in KO cMyc$^+$ LZ GC-B cells.

The reduction of K36me2 levels was specific to DNA replication-dependent histone H3.1 and was not observed in DNA replication-independent histone H3.3 (**Fig. 2B**). This suggests that cell division is required for the depletion of H3K36me2. Previous studies have indicated that the loss of H3K36me2 is associated with a decrease in acetylation of histone H3 at K27 (K27ac) (*40*). There was decreased K27ac on histone H3.1 in KO LZ GC-B cells relative to WT cells, while no such change was observed on histone H3.3 (**Fig. 2B**). The decrease in K36me2 on histone H3.1 may lead to increased levels of monomethylated K36 (K36me1) on histone H3.1. While no elevation of K36me1 was detected on histone H3.1 in KO LZ GC-B cells relative to their WT cells, a significant increase in this histone PTM was observed in KO DZ GC-B cells compared to their WT counterparts (**Fig. 2B** and ***Supplemental Figure 2B***). This could be attributed to the migration of dividing LZ GC-B cells to the DZ, where chromatin marks could potentially be deposited on newly synthesized histones. Apart from K36me1, no other changes were observed in the histone PTMs at K36 of histone H3.1 in DZ GC-B cells between WT and KO cells (***Supplemental Figure 2B***). These findings suggest that miR-155 regulates the levels of K36me2 of H3.1 during cell division in LZ GC-B cells. Given that LZ GC-B cells are generally quiescent, these dividing cells likely represent cMyc$^+$ LZ GC-B cells (*7*).

To examine the effect of miR-155-mediated regulation on histone H3K36me2 levels in cMyc$^+$ GC-B cells, we performed immunostaining of spleen sections from SRBC-immunized, *Mir155*-sufficient and *Mir155*-deficient mice. Within the GL7-positive GC areas, a correlation in co-expression of MYC and H3K36me2 was observed in both groups to some extents (**Fig.2C** and **Fig.2D**). However, the Pearson's correlation coefficients with 95% confidence interval showed no overlap between the values of WT and KO groups ($r = 0.574 – 0.596$ and $0.344 – 0.384$, for WT and KO, respectively), indicating a stronger correlation in the WT group than the KO group (**Fig.2D**). To investigate the difference in H3K36me2 levels between WT and KO MYC$^+$ GC-B cells, we compared the relative mean intensity of H3K36me2 in cells within the top 5% of MYC positive cells from the total cell population shown in **Fig.2D**. The analysis revealed a significant reduction in H3K36me2 levels in KO MYC$^+$ GC-B cells compared to the corresponding WT cells (**Fig.2E**), which is consistent with the results derived from the MS analysis (**Fig.2B**). We also performed immunofluorescence-based correlation analysis between MYC and H3K36me1 or H3K36me3. However, the correlation in co-expression of MYC and these histone PTMs exhibited only minor variations when comparing KO and WT MYC$^+$ GC-B cells (***Supplemental Figure 2C and 2D***). These results suggest that the co-expression pattern between MYC and H3K36me1 or H3K36me3 remains largely unchanged, unlike the substantial changes observed in H3K36me2. Collectively, these results provide compelling evidence for the crucial role of miR-155 as an

epigenetic modulator in histone PTMs. Notably, miR-155 predominantly regulates the levels of H3K36me2 in dividing cMyc$^+$ LZ GC-B cells, potentially influencing mitochondrial functions in GC-B cells.

MiR-155 primarily controls Kdm2a expression in high affinity cMyc$^+$ LZ GC-B cells.

Demethylation of H3K36me2 can be catalyzed by the lysine demethylases (KDMs), *Kdm2a*, *Kdm2b*, *Kdm4a*, *Kdm4b* and *Kdm4c* (*41*). We examined whether any of mRNAs encoding these enzymes was differentially expressed between WT and KO cMyc$^+$ LZ GC-B cells. Expression of *Kdm2a* was significantly higher in KO cMyc$^+$ LZ GC-B cells compared to WT cMyc$^+$ LZ GC-B cells, while the others (*Kdm2b*, *Kdm4b* and *Kdm4c*) exhibited similar expression levels between the two groups (**Fig.3A**). In contrast, the expression of *Kdm4a* was found to be decreased in KO cMyc$^+$ LZ GC-B cells compared to WT cMyc$^+$ LZ GC-B cells (**Fig.3A** and ***Supplemental Table 2***). Next, we examined whether *Kdm2a* mRNA is predicted as a target of miR-155. By utilizing miR prediction tools, we identified *Kdm2a* as one of the 18 genes that were predicted to be targets of miR-155 and showed differential expression between WT and KO cMyc$^+$ LZ GC-B cells (***Supplemental Figure 3A*** and ***Supplemental Table 2***). *Kdm2a* has one 8-mer miR-155-binding site at 3' UTR that is conserved across multiple species, including human, mouse, and rat (**Fig.3B**).

To investigate the relationship between KDM2A and miR-155, we examined the co-expression of KDM2A and MYC by immunostaining tissue sections derived from *Mir155*-sufficient and *Mir155*-deficient mice using antibodies against IgD, MYC and KDM2A. This revealed a strong correlation in co-expression of these two proteins in both groups (r = 0.775 – 0.788 and 0.720 – 0.740, for WT and KO, respectively) (**Fig.3C** and **3D**). Therefore, we concluded that KDM2A is mainly expressed in positively selected cMyc$^+$ GC-B cells. To examine the degree and cell subpopulations expressing KDM2A, we performed flow cytometric analysis of GC-B cells derived from SW_{HEL} adoptive transfer system. In WT mice, the analysis revealed a ~1.3-fold increase in KDM2A expression in cMyc$^+$ LZ GC-B cells compared to cMyc$^-$ LZ GC-B cells (**Fig.3E**), indicating that positive selection signals can induce its expression. The highest expression of KDM2A was observed in cMyc$^+$ DZ GC-B cells. A similar expression pattern was observed in KO GC-B cell subpopulations. In all GC-B cell subpopulations, KDM2A expression was significantly higher in KO cells compared to their WT counterparts (**Fig.3E** and ***Supplementary Figure 3B***).

The SW_{HEL} system enables the distinction between high and low affinity B cells following $HEL^{3\times}$ immunization. When comparing high and low affinity clones within each WT GC-B cell subpopulation, there were no significant differences in the level of KDM2A (**Fig.3F**). In contrast, the lack of miR-155 led to a substantial increase of KDM2A expression in high affinity clones compared to low affinity clones within the cMyc$^+$ LZ GC-B cell subpopulation. As a result, there was a marked elevation in KDM2A expression in high affinity clones of KO cells compared to WT cells (**Fig.3F**). Collectively, these results suggest that KDM2A is preferentially induced in

high affinity clones within the cMyc$^+$ LZ GC-B cell subpopulation during positive selection, and therefore, miR-155 is required to dampen KDM2A expression in these cells.

Hypoxia induces KDM2A in LZ GC-B cells.

Hypoxia induces *Kdm2a* expression at both transcript and protein levels (*42, 43*). Given that previous studies have shown that the LZ of GCs is hypoxic (*10-12*), we hypothesized that miR-155 counteracts the hypoxia-induced increase of KDM2A expression: i.e., in the absence of miR-155, KDM2A expression is enhanced under hypoxic conditions. Since the concept that the LZ has a more hypoxic microenvironment than the DZ remains a subject of controversy (*8, 44*), we quantified the degree of hypoxia that GC-B cells were experiencing using the hypoxia detecting dye, MAR (see materials). Flow cytometric analysis revealed that a bimodal distribution of MAR fluorescence intensity in non-GC-B cells. This potentially reflects their location within the tissue, as it is generally considered that regions adjacent to blood vessels are less hypoxic, whereas areas distant from blood vessels experience more hypoxia (*45*). Here, LZ GC-B cells exhibited higher MAR fluorescence intensity than DZ GC-B cells (**Fig.4A**), indicating greater levels of hypoxia, in line with previous studies (*10-12*).

To examine the effect of hypoxia on KDM2A expression in B cells, we cultured splenic B cells in the presence of anti-IgM, anti-CD40 and IL-4, which mimicked the combination of positive selection signals derived from BCR and T cell help. These cells were cultured in either normal oxygen concentration (21%, normoxic) or low oxygen concentration (1%, hypoxic), and KDM2A expression was examined by flow cytometry. Following a two-day activation with positive selection mimics under normoxic conditions, both WT and KO B cells showed increased KDM2A expression (**Fig.4B**). However, there was no significant difference in KDM2A levels between WT and KO cells under normoxic conditions (**Fig.4B**). Under hypoxic conditions, the expression of KDM2A was markedly increased, resulting in higher expression of KDM2A in both WT and KO B cells compared to normoxic conditions (**Fig.4B**). By contrast, in hypoxic cultures, KDM2A expression was ~1.6-fold greater in the KO B cells than WT B cells (**Fig.4B**). This difference in expression was attributed to the increased expression of miR-155 under hypoxic conditions (***Supplemental Figure 4A***), consistent with previous reports (*46, 47*). Therefore, hypoxia was necessary for observing differential levels of KDM2A between KO and WT *in vitro* cultured B cells. These findings suggest that miR-155 exerts a strong repressive effect on *Kdm2a* primarily under hypoxic conditions.

The regulatory activity of miR-155 is revealed under hypoxia.

To examine the impact of hypoxia on cell division, we cultured CellTraceViolet (CTV)-labeled B cells from *Mir155*-sufficient and *Mir155*-deficient mice with positive selection mimics in either normoxic or hypoxic conditions. As expected, hypoxia suppressed cell proliferation regardless of genotype (**Fig.4C**). However, whereas both WT and KO cells showed similar levels of division

in normoxic cultures, miR-155 KO B cells exhibited significantly less division than WT B cells under hypoxic conditions (**Fig.4C**). The results highlight the critical role of miR-155 for cell proliferation under hypoxic conditions.

To investigate the influence of hypoxia on mitochondrial ROS production, we used non-fluorescent MitoTracker Orange CM-H_2 TMRos that becomes fluorescent upon oxidization. After a two-day culture period under either hypoxic or normoxic conditions, we stained WT and KO B cells with MitoTracker dyes. WT B cells produced lower amounts of mitochondrial ROS under hypoxic conditions (**Fig.4D** and **Fig.4E)**. In contrast, hypoxic KO cultures had significantly higher amounts of mitochondrial ROS than normoxic KO cultures (**Fig.4D** and **Fig.4E**), indicating mitochondrial dysfunction in these cells. Consequently, KO B cells exhibited a significantly increased ROS production compared to WT B cells under hypoxic conditions, while no such difference was observed under normoxic conditions (**Fig.4D** and **Fig.4E**). To further investigate mitochondrial integrity in KO B cells, we assessed energy metabolic states coupled to mitochondrial functions. To this end, we measured the abundance of adenosine triphosphate (ATP) produced through metabolic processes. After two days of culturing WT and KO B cells under either normoxic or hypoxic conditions, we further cultured the cells in the following media supplemented with either glucose, glucose plus oligomycin, galactose, or galactose plus oligomycin. To directly compare energy metabolic capacities of cells, all cells were cultured in hypoxic conditions for 2 hours using the indicated media. Cells can use both glycolysis and OXPHOS to produce ATP when cultured in glucose-supplemented medium, while in medium supplemented with glucose and oligomycin, an inhibitor of OXPHOS, cells rely solely on glycolysis for ATP production. Under hypoxic conditions, both WT and KO cells exhibited a reduction of ATP abundance when cultured in glucose-supplemented medium, compared to their normoxic counterparts (***Supplemental Figure 4B***). This result is consistent with previous reports showing reduced energy production under hypoxia (*48, 49*). When B cells were cultured in medium supplemented with both glucose and oligomycin, the relative abundance of ATP was similar to corresponding cultures supplemented with glucose alone across all cell types (**Fig.4F**), indicating that the cells were able to survive by relying on their glycolytic capacity without the need for OXPHOS, in accordance with the well-known "Crabtree effect" (*50, 51*). In contrast, cells cultured in galactose must use OXPHOS to generate ATP (*52*). In this culture condition, we observed a reduction in ATP abundance in both WT and KO B cells under hypoxia compared to normoxia.

Furthermore, while ATP production through OXPHOS was compromised in hypoxic cultures of both WT and KO cells, the impairment was more severe in KO B cells (**Fig.4F**). ATP production was abrogated when WT or KO B cells were cultured in medium containing galactose and oligomycin regardless of oxygen tension (**Fig.4F**). These results suggest that miR-155 plays a critical role in the metabolic reprogramming of activated B cells by regulating OXPHOS under hypoxic conditions. Collectively, the results demonstrate that the regulatory activity of miR-155 in modulating mitochondrial function and energy metabolism in activated B cells is manifested in a hypoxic environment.

MiR-155 optimizes nuclear mitochondrial gene expression through KDM2A-mediated control of H3K36me2 levels.

To investigate how *Mir155*-deficiency impacts genome-wide binding of KDM2A and H3K36me2 distribution, we performed ChIP-seq assays using hypoxic B cell cultures. The genomic distribution of KDM2A and H3K36me2 peaks showed significant differences between WT and KO B cells (**Fig.5A**). In KO B cells compared to WT B cells, there was a proportional increase in KDM2A peaks within the promoter/transcriptional start site (TSS) regions (WT = 26.5%, KO = 34.5%), accompanied by a concurrent reduction of H3K36me2 peaks in the same regions (WT = 4.59%, KO = 3.77%) (**Fig.5A**). Consistent with a previous report showing that KDM2A preferentially binds to CGIs islands (CGIs) primarily located at gene promoters (*53*), we detected significant enrichment of KDM2A peaks specifically at the TSS-proximal regions of genes containing CGIs (**Fig.5B**). Furthermore, we observed a concurrent depletion in H3K36me2 signals within these regions of CGI containing genes in both WT and KO B cells (**Fig.5B**). To identify distinctive patterns of KDM2A binding and H3K36me2 marks, we examined the peak positions in relation to the nearest TSS (**Fig.5C**). These plots revealed that a higher density of KDM2A peaks in KO B cells at TSS-proximal regions compared to WT B cells (**Fig.5C**). Accordingly, H3K36me2 peak density was reduced in KO B cells relative to WT B cells at these same regions and in the intragenic regions proximal to the TSS (**Fig.5C**). Our findings indicate that the absence of miR-155 leads to an elevated expression of KDM2A, which in turn triggers enhanced binding of KDM2A to TSS-proximal regions and a concomitant depletion of H3K36me2 in those regions as well as in the intragenic regions.

To elucidate the biological functions of genes bound by KDM2A, we investigated the KDM2A target genes that displayed differential binding between WT and KO B cells and identified "WT-enriched" and "KO-enriched" KDM2A peaks (***Supplemental Table 3***). Functional annotation clustering analysis with DAVID (*54*) showed that genes with "WT-enriched" or "KO-enriched" Kdm2a peaks were strongly associated with the regulation of mitochondrial functions (**Fig.5D**). These results suggest that KDM2A plays a role in regulating the expression of nuclear mitochondrial genes during hypoxia. Among the genes with "WT-enriched" and "KO-enriched" KDM2A peaks, we identified 102 and 30 genes encoding nuclear mitochondrial proteins listed in MitoCarta 3.0 (*55*), respectively. The nuclear mitochondrial genes identified with "WT-enriched" KDM2A peaks did not overlap with those identified with "KO-enriched" KDM2A peaks. This indicates that KDM2A's binding pattern is altered in KO B cells, potentially due to its overexpression. Bulk RNA-seq analysis showed that five mitochondrial genes with "KO-enriched" KDM2A peaks at promoter/TSS regions and two mitochondrial ribosomal proteins with "KO-enriched" KDM2A peaks at the first intron, which corresponds to the intragenic regions proximal to the TSS, were reduced in their expression in KO cMyc$^+$ LZ GC-B cells compared to WT cMyc$^+$ LZ GC-B cells (**Fig.5E** and ***Supplemental Table 3***). These findings suggested that the differential binding of KDM2A between WT and KO B cells affected the expression of nuclear mitochondrial genes. Furthermore, among the five genes with "KO-enriched" KDM2A peaks located in the promoter/TSS regions, *Ndufv3* and *Atp5l* are known to play an essential role in OXPHOS (*55*).

Thus, the miR-155-*Kdm2a* axis has a critical function in regulating OXPHOS coupled with mitochondrial bioenergetic functions in activated B cells under hypoxic conditions.

The miR-155-Kdm2a interaction regulates mitochondrial ROS and apoptosis in GC-B cells.

To validate the regulatory interaction of the miR-155-*Kdm2a* axis, we generated mice with a mutated miR-155 binding site in the 3'UTR of *Kdm2a* (**Fig.6A**). B cell development was normal in homozygous mutant (hereafter called "MUT") mice (***Supplemental Figure 5A***). WT and MUT mice were immunized with SRBCs, and KDM2A expression in GC-B cells was assessed by flow cytometry. In LZ GC-B cells of MUT mice, KDM2A expression exhibited a ~1.2-fold increase relative to their WT littermates (**Fig.6B**). No significant difference in KDM2A expression was observed in DZ GC-B cells. These results indicate that miR-155 limits *Kdm2a* expression in LZ GC-B cells through its binding site on Kdm2a mRNA. To examine B cell-intrinsic effects of the mutation, we performed adoptive transfer experiments by transferring B cells isolated from the spleens of either WT or MUT mice into μMT mice, which lacks mature B cells (*56*). The mice were then immunized with SRBCs. Seven days later, all recipient mice gave rise to GC-B cells, but the total number of DZ GC-B cells was reduced by ~29% in the MUT background compared to that of WT, while the number of LZ GC-B cells was similar between WT and MUT mice (**Fig.6C** and ***Supplemental Figure 5C***).

We investigated the impact of the 3'UTR mutation on mitochondrial ROS and apoptosis in GC-B cells by transferring B cells into μMT mice. The proportion of MitoSOX$^+$ cells was higher in both LZ and DZ GC-B cells of MUT mice compared to WT (**Fig.6D**). Moreover, the percentage of active-Caspase3$^+$ cells were increased in DZ GC-B cells of MUT mice, when compared to WT mice (**Fig.6E**). The elevated apoptosis in GC-B cells from MUT mice compared to WT mice provides an explanation for the decreased number of DZ GC-B cells depicted in **Fig.6C**. These results largely mirror the observations in *Mir155*-deficient mice. Moreover, the overexpression of KDM2A in GC-B cells through lentiviral transduction resulted in an increased percentage of MitoSOX$^+$ DZ GC-B cells compared to control cells (***Supplemental Figure 5D***). Taken together, these findings underscore the crucial role of miR-155 in repressing *Kdm2a* to counteract the effects of hypoxia during the positive selection process.

Discussion

We demonstrated that miR-155 critically regulates H3K36me2 levels by directly repressing histone demethylase *Kdm2a* during GC positive selection. This repression enabled GC-B cells to remodel their mitochondria and to proliferate in the hypoxic LZ microenvironment. Maintaining mitochondrial fitness during positive selection in the LZ was essential for GC-B cells to continue vigorous proliferation in the DZ. In the absence of miR-155, dysfunctional mitochondria led to increased ROS production and subsequent apoptosis in GC-B cells (**Fig.7**).

While *Mir155*-defcient mice show a compromised proliferation of GC-B cells, *in vitro* cultured KO B cells exhibit normal DNA synthesis and cell proliferation rates regardless of stimuli (*57-59*). Thus, it was unclear why these *in vitro* cultured B cells cannot recapitulate the phenotype observed *in vivo*. In this study, we demonstrated that essential function of miR-155 is revealed under hypoxia *in vitro* and reproduced the known *in vivo* phenotypes observed in KO B cells. We have identified *Kdm2a* as a critical target gene of miR-155, which is induced under hypoxic conditions. *Kdm2a* exhibits context-dependent effects on proliferation (*21, 22*) and may act as a negative regulator of proliferation in GC-B cells. Therefore, miR-155-mediated *Kdm2a* repression enabled GC-B cells to initiate cell division under hypoxic conditions in the LZ during positive selection.

Our findings demonstrated the critical role of miR-155 in facilitating the metabolic adaptation of positively selected GC-B cells for cell division while mitigating hypoxia-driven stress in the LZ. Our previous studies have shown that high-affinity clones display greater proliferative activity than low-affinity clones within cMyc$^+$ LZ GC-B cell subpopulation (*7*). Indeed, miR-155 exerted its most potent suppressive effect on *Kdm2a* especially within the high-affinity clones of the cMyc$^+$ LZ GC-B cell subpopulation (**Fig.3F**). In agreement with this, *Mir155*-deficient mice exhibit a selective loss of high-affinity GC-B cells due to apoptosis (*26, 58, 59*). In the absence of miR-155, cMyc$^+$ LZ GC-B cells with higher levels of KDM2A experience detrimental effects such as increased ROS production due to dysfunctional mitochondrial and subsequent cell death (**Fig.1B**, **Fig.6D** and **Fig.6E**). Despite the downregulation of miR-155 expression in cMyc$^+$ DZ GC-B cells and its absence in cMyc$^-$ DZ GC-B cells, there was a persistent increase in ROS production in these cells when miR-155 was absent. This may be because DZ GC-B cells prioritize energy use for mitosis rather than mitochondrial repair. Therefore, GC-B cells appear to be incapable of restoring mitochondrial function after migration to the DZ. The findings underscore the importance of the miR-155-*Kdm2a* regulatory axis in the LZ, which promoted metabolic reprogramming and gradual enhancement of OXPHOS in positively selected GC-B cells. As a result, positively selected GC-B cells could cope with the higher rate of cell division in the DZ by utilizing ATP provided by OXPHOS in remodeled mitochondria. These results are consistent with a previous observation that GC-B cells with higher affinity require increased OXPHOS activity to undergo extensive proliferation (*9*).

KDM2A expression was upregulated >1.5-fold in *Mir155*-KO mice compared to WT mice in both cMyc$^+$ and cMyc$^-$ DZ GC-B cells (**Fig. 3E**). However, the expression level of KDM2A in DZ

GC-B cells of MUT mice was comparable to that of WT mice. Firstly, there is evidence for a 6-mer miR-155 binding site in the 3'UTR of mouse *Kdm2a* (*60*). Since this 6-mer binding site is intact in MUT mice, miR-155 may partially repress *Kdm2a* transcripts through this region, inhibiting the KDM2A elevation in MUT mice. Alternatively, other miR-155 target(s) could contribute to the induction of KDM2A. *Hif1a* can be directly targeted by miR-155 (*60*) and potentially influences the expression of KDM2A because KDM2A may be induced partially in a HIF-1α-dependent manner under hypoxic conditions (*42*). Given that *Hif1a* is repressed by miR-155 in a similar manner in both WT and MUT mice, the lower HIF-1α expression in MUT B cells compared to KO B cells may limit the efficiency of KDM2A induction in MUT mice.

MiRs generally have multiple targets. We identified 18 mRNAs that are predicted miR-155 targets in cMyc$^+$ LZ GC-B cells and exhibit increased expression in the absence of miR-155 (***Supplemental Figure 3A***). One of the molecules, *Jarid2* was previously discovered as a miR-155 target in positively selected GC-B cells, and its overexpression has been shown to increase apoptosis in LZ GC-B cells (*26*). JARID2 functions as an accessory component of the Polycomb Repressive Complex 2 (PRC2), which catalyzes H3K27me3 (*61*), thereby epigenetically regulating gene expression. Therefore, the modulation of PRC2 activity by JARID2 potentially contributes to elevated apoptosis in these cells. Another molecule, F-Box Only Protein 11 (*Fbxo11*), was also among the identified 18 genes, and is a part of a multi-subunit E3 ubiquitin-ligase protein complex that catalyze the ubiquitination of proteins destined for proteasomal degradation. GC-B cell-specific deletion of *Fbxo11* increases the number of GC-B cells, particularly DZ GC-B cells, suggesting that this molecule is associated with GC-B cells proliferation (*62*). Therefore, the phenotypic alterations observed in *Mir155*-deficient mice may result from the cumulative effects of several causal targets acting together with *Kdm2a*.

Collectively, our findings demonstrate that miR-155 acts as an epigenetic regulator to limit the activity of *Kdm2a* on target genes, thereby maintaining appropriate levels of H3K36me2. The precise control of H3K36me2 levels during positive selection is vital for the optimal expression of nuclear mitochondrial genes in GC-B cells under hypoxic conditions, thus facilitating mitochondrial remodeling. The resultant metabolic reprogramming is indispensable for the survival and robust proliferation of GC-B cells within the DZ. Our findings provide insights that could pave the way for the development of novel therapeutics targeting histone PTMs to control GC responses in the context of vaccination and lymphomagenesis.

Materials and Methods

Mice

Mir155-deficient mice (*57*), SW_{HEL} mice (*27*), *Myc*$^{gfp/gfp}$ mice (*28*), *Aicda-cre*-h*CD2* (*29*), µMT (*56*) and B6SJL CD45.1 mice were maintained on C57BL/6J background. SW_{HEL} mice were interbred with *Myc*$^{gfp/gfp}$ and *Aicda-cre*-h*CD2* mice and were maintained either *Mir155*-sufficient or *Mir155*-deficient background. B6SJL CD45.1 mice were crossed with C57BL/6J, and heterozygous mice were used. 6–15-week-old male and female mice were used. For the generation of *Kdm2a* mutant mice, a single guide RNA (AAATTAAATGTAAGCATTAA) was designed using CRISPOR (http://crispor.tefor.net/) to cut in the 3'UTR of the *Kdm2a* gene (Position 3369 – 3376 of *Kdm2a* 3'UTR, ENST00000398645.2). A 111bp ssODN (CTTATTTAGAGTCGATCTCCAATGTTGTGCTAAGATTTTTAAATTAAATGTAAGatgc AtGGGAATGAGTCTTAGGCCACCAGCTGACACATTGGCATTATTTTGGGTCAG) was designed containing the "mir155-2" mutation. Zygotes were generated by superovulation of C57BL/6J mice and electroporated with 50 µL of Cas9 protein / sgRNA / ssODN (final concentrations 1.2 µM / 6 µM / 8 µM respectively). Both template and guide were added at the 1 cell stage. Electroporation of the embryos was performed using a Nepa21 electroporator (Sonidel). Two males (1 heterozygous and 1 homozygous) were found to have sequence perfect integration of the mir155-2 mutation via Sanger sequencing (Forward primer: CGAGGACGTAGAACATGCGA, Reverse primer: GGGCAGGCACTTCCTAGTTT) and were further bred to C57BL/6J yielding 2 heterozygous F1s. Q-PCR CNV analysis further confirmed the presence of only one copy of the mir155-2 mutation. F1 mice were inbred to generate homozygous mutant mice. All mice were bred and kept under specific-pathogen-free conditions at the Francis Crick Institute Biological Research Facility in accordance with guidelines set by UK Home Office and the Francis Crick Institute Ethical Review Panel.

Immunization, treatments, and adoptive transfers

Mice were immunized intraperitoneally with 2×10^8 SRBCs. For HEL-specific GC responses, splenic cells from donor mice were incubated with biotinylated antibodies: anti-CD43 (S7; BD Biosciences), anti-CD4 (GK1.5; BioLegend) and anti-Ter-119 (TER-119; BioLegend), washed and incubated with anti-biotin microbeads (Miltenyi Biotec). B cells were enriched by biotin negative selection using MACS LS Columns (Miltenyi Biotec). The purity of recovered $CD19^+$ $B220^+$ B cells was >97%. 5×10^4 to 1×10^5 HEL-specific B cells were transferred into B6SJL $CD45.1^+$ hosts intravenously. Mice were immunized intraperitoneally on the same day of cell transfer or one day later with 2×10^8 SRBCs conjugated with $HEL^{3\times}$. The HyHEL10 BCR of SW_{HEL} mice exhibits a binding affinity 13,000-fold lower to $HEL^{3\times}$ than to HEL. Immunization with $HEL^{3\times}$ induces robust and persistent GC responses at the expense of extrafollicular responses (*63*). $HEL^{3\times}$ protein was harvested from the supernatant of Chinese hamster ovary (CHO) cells expressing his-tagged $HEL^{3\times}$ (*64*) and was purified using a His-Trap FF column (Cytiva) on AKTA Pure column chromatography system (Cytiva). Eluted protein was concentrated to 0.5 ml (Vivaspin 15, 10,000 Da cutoff concentrator) and applied to a S200 10/300 analytical size exclusion column (Cytiva). $HEL^{3\times}$ was found to eluted as a single, symmetrical peak and snap frozen at 1 mg/ml and stored at -80 °C until required. For B cell transfer from wild type (*Kdm2a-*

mutant littermates) or *Kdm2a*-mutant mice, splenic B cells from donor mice were enriched by negative selection using MACS LS Columns as described above. 2.5×10^7 to 3×10^7 B cells were transferred into μMT hosts intravenously. Mice were immunized intraperitoneally on the same day of cell transfer with 2×10^8 SRBCs. To detect hypoxia, the hypoxia dye MAR was used. MAR is non-fluorescent compound that is irreversibly converted into a fluorescent molecule by a reductase that is activated in response to low oxygen concentrations. The conversion of MAR only occurs under hypoxic conditions (*65*), and the fluorescence of MAR is not affected by increased oxygen concentrations during tissue processing. Eight days after subcutaneous immunization of C57BL/6 mice with 50 μg of 4-Hydroxy-3-nitrophenyl acetyl hapten conjugated chicken gamma globulin (NP-CGG) in Imject Alum Adjuvant (ThermoFisher Scientific), 4.3 μg MAR hypoxia detecting probe (Goryo Chemical) in PBS per site or control DMSO in PBS was subcutaneously injected into two sites around the immunized inguinal lymph node. Three hours later, lymph nodes were harvested for flow cytometric analysis.

Flow cytometry and cell sorting

Multicolour flow cytometry for analyses or for cell sorting was performed on LSR Fortessa or FACSAria (BD Biosciences) and data were analyzed using FlowJo v.10.8.1 software. PBS + 2% FBS was used as flow cytometry buffer. Harvested splenic B cells were enriched by CD43, Ter119 and CD4 biotin negative selection using MACS LS Columns to remove $CD43^+$ plasmablasts and non-B cells for analysis. For HEL-specific GC responses, splenic B cells were enriched by CD45.1 negative selection using MACS LS Columns to remove recipient-derived cells. Single-cell suspensions were prepared and stained for the antibodies specific for cell surface markers. HEL-binding cells were stained with HEL (50 ng/ml), followed by HyHEL9 Alexa Fluor 647. For active-caspase 3 staining, after surface marker staining, cells were fixed and permeabilized using a Fixation/Permeabilization Solution Kit (BD Biosciences) and stained with anti-active caspase 3 antibody (BD Biosciences). For KDM2A staining, cells were stained for surface marker antibodies, and were fixed and permeabilized using a True-Nuclear Transcription Factor Buffer Set (BioLegend). The permeabilized cells were stained with anti-KDM2A antibody (Abcam), followed by donkey anti-rabbit antibody staining. Cells stained with an anti-rabbit antibody, but no primary antibodies determined the basal level of fluorescence intensity for KDM2A, and the basal fluorescence intensity was subtracted from each MFI of KDM2A staining for the calculation of relative MFI. For MitoSOX detection, cells were stained for surface marker antibodies. Then, they were incubated in HBSS with Calcium and Magnesium (ThermoFisher scientific) supplemented with 2.5 μM MitoSOX Red (ThermoFisher Scientific) and 50 nM Mito Tracker Deep Red FM (ThermoFisher Scientific) for 20 - 30 min and washed as described by the manufacturer before analysis. All the antibodies used for the study are listed in ***Supplemental Table 4***.

B cell culture, proliferation assays and ATP measurement

Harvested splenic B cells from *Mir155*-sufficient or *Mir155*-deficient C57BL/6 mice were enriched by CD43, Ter119 and CD4 biotin negative selection using MACS LS Columns. Purified B cells were cultured with positive selection mimicking stimulants (1 μg/ml anti-CD40 antibody (HM40-3), 5 μg/ml AffiniPure $F(ab')_2$ Fragment Goat Anti-Mouse IgM (H+L) (Jackson

ImmunoResearch) and 4 ng/ml murine IL-4 (PeproTech) in B cell medium (RPMI 1640 GlutaMAX Supplement medium supplemented with 10 % fetal bovine serum, 1 % pen-strep solution and 50 μM β-mercaptoethanol) at 37 °C in a humidified chamber containing 5% CO_2 and either 21% O_2 (normoxia) or 1% O_2 (hypoxia). For CTV proliferation assays, purified B cells were stained with 5μM CellTrace Violet (ThermoFisher Scientific) in PBS for 15 min at RT and washed as described by the manufacturer. For ATP measurement, purified B cells were cultured for 2 days as described above. On the measurement day, cells were washed twice in PBS to remove glucose and resuspended in either glucose medium (DMEM no glucose medium supplemented with 1 % pen-strep solution, 50 μM β-mercaptoethanol and 10 mM D-(+)-glucose (Merck)) or galactose medium (DMEM no glucose medium supplemented with 1 % pen-strep solution, 50 μM β-mercaptoethanol and 10 mM galactose (Merck)). After a thorough wash to remove glucose in the medium, 1×10^5 cells were plated per well and were further cultured in the presence or absence of 5 μM oligomycin (Merck) at 37 °C in a humidified chamber containing 5% CO_2 and 1% O_2 for 2 hours. All the cells were cultured in hypoxic conditions for 2 hours to directly compare ATP production ability under the same condition. ATP was measured with Mitochondrial ToxGlo Assay kit (Promega) and followed the manufacturer's protocol.

Immunofluorescence

Harvested spleens were embedded in OCT compound. 9 μm cryosections were fixed in ice cold acetone for 3 min, followed by air dry for 20 min. The sections were blocked with blocking buffer (0.3% Triton X-100, 1% BSA, 5% normal bovine serum and 1% rabbit serum in PBS) and stained with the antibodies listed in ***Supplemental Table 4*** for overnight at 4 C°. For MitoTracker staining of cultured B cells, purified B cells were cultured for 2 days as described above and washed in PBS twice. Cell suspension containing 2-3 $\times 10^6$ cells/ml in PBS was placed on Shi-fix coverslips (Shikhar Biotech) and incubated at 37 °C in a humidified chamber containing 5% CO_2 and 1% O_2 for 30 - 40 min. The coverslips were then washed as instructed by the manufacturer. Cells bound on the coverslips were stained with 83 nM MitoTracker Orange CM-H_2TMRos (ThermoFisher Scientific) and 50 nM Mito Tracker Deep Red FM at 37 °C for 15 min, followed by wash in warm PBS and fixation with 4% formaldehyde (ThermoFisher Scientific). Slides were mounted with Prolong Gold Antifade Reagent with DAPI (ThermoFisher Scientific) and analyzed using LSM880 (Zeiss).

Image analysis

For the detection of mitochondrial ROS on confocal images of in vitro cultured B cells, the ratiometric cytoplasmic-to-nuclear intensity of mitochondrial ROS was quantified using a custom-built CellProfiler (v. 4.2.5) (*66*) pipeline. Uneven illumination was first corrected in the Mito Tracker Deep Red FM and MitoTracker Orange CMTMRos channels by dividing the pixel values by a polynomial fit to the intensity of the image pixels. Following smoothing with median filtering, objects were then detected in the DAPI and Mito Tracker Deep Red FM channels using minimum cross-entropy (Mito Tracker Deep Red FM) or Otsu (DAPI) thresholding. All objects detected in the DAPI channel are then associated with corresponding objects in the Mito Tracker Deep Red FM channel, i.e., any Mito Tracker Deep Red FM objects without any corresponding DAPI objects are removed. The cytoplasm was then defined as the area within Mito Tracker Deep

Red FM objects not occupied by DAPI objects. The mean intensity in the MitoTracker Orange CMTMRos channel was then measured within each cytoplasm object, and this was divided by the background value, the mean intensity in the MitoTracker Orange CMTMRos channel of each DAPI object to minimize batch effects. For the analysis of co-expression of histone PTMs (H3K36me1, 2 or 3)/MYC and MYC/KDM2A in spleen sections was quantified using a custom FIJI script (*67*). First, the approximate centers of cells were detected by identifying local extrema in eigenvalues of the Hessian tensor, calculated based on the IgD channel using FeatureJ (https://imagescience.org/meijering/software/featurej/hessian/). Cells were then fully segmented using these detected centers of cells as "markers" in a marker-controlled watershed operation, implementing using MorphoLibJ (*68*), using a Gaussian- then Sobel-filtered version of the IgD channel as input. The mean intensity of histone PTMs, MYC or KDM2A within the segmented cells was then quantified using ImageJ FIJI (v. 2.9.0). All cells outside a manually defined region of interest were excluded.

Analysis of Histone PTMs

Cells were prepared for sorting by flow cytometry as described above. LZ or DZ GC-B cells (> 1×10^5) were directly sorted into 2 N H_2SO_4 as previously described (*36*). After a 30 min incubation at room temperature, cellular debris was removed by centrifugation at 4,000 × g for 5 min and histones were precipitated from the supernatant with trichloroacetic acid at a final concentration of 20% (v/v) overnight at 4 °C. Precipitated histones were pelleted with centrifugation at 10,000 × g for 5 min at 4 °C, washed once with 0.1% HCl in acetone, then once with 100% acetone with centrifugation at 15,000 × g for 5 min at 4 °C. Histones were briefly dried with SpeedVac concentrator (Eppendorf) and stored at -80 °C until derivatization. Histones were propionylated and digested according to Garcia *et al.* (*37*), with the modification of a single round of propionylation for 1 hr prior to and following digestion. Targeted LC-MS/MS was performed on a Thermo TSQ Quantiva (ThermoFisher Scientific). All injections were performed in technical triplicate. Raw data were analyzed with Skyline (v. 21.2) according to published methods (*36*). The relative abundance of each histone PTM was calculated from the total peak areas exported from Skyline. All the chemicals were purchased from ThermoFisher Sceintific.

RNA-seq and data analysis

Mir155-sufficient or *Mir155*-deficient cMyc-GFP$^+$ LZ GC-B cells were sorted by flow cytometry 5 days after HEL$^{3\times}$-SRBC immunization. Total RNA was prepared with TRIzol Reagent (ThermoFisher Scientific) combined with RNeasy Mini Kit (QIAGEN) and processed using a TruSeq Stranded mRNA Sample Prep kit (Illumina). RNA-sequencing was carried out on the Illumina HiSeq 2500 platform and generated ~43 million, 75 bp paired-end reads per sample. The RSEM package (v. 1.2.31) (*69*) in conjunction with the bowtie2 alignment algorithm (v. 2.2.9) (*70*) was used for the mapping and subsequent gene-level counting of the sequenced reads with respect to Ensembl mouse GRCm.38.86 version transcriptome. Normalization of raw count data and differential expression analysis was performed with the DESeq2 package (v. 1.24.1) (*71*) within the R programming environment (v. 3.6.0). Differentially expressed genes were defined as those showing statistically significant differences between KO and WT sample groups (FDR <0.05). Majority of *Mir155*-deficient donor mice were males, whereas majority of *Mir155*-

sufficient donor mice were female. Thus, the following 4 genes that are in the Y chromosome and more enriched in KO than WT mice were removed from the list of DEGs (ENSMUSG00000069045, ENSMUSG00000069049, ENSMUSG00000056673 and ENSMUSG00000068457). Gene list ranked by the Wald statistic were used to look for pathway and biological process enrichment using the Broad's GSEA software (v2.1.0) with gene sets from MSigDB (v6) (*72*). GSEA results were visualized with EnrichmentMap (3.3.4) (*73*) in Cytoscape (v3.7). We employed three miR target prediction tools, MiRDB (*74*), Diana (*75*) and Target scan (*76*) for identifying miR-155 targets.

scRNA-seq and data analysis

Donor-specific *Mir155*-sufficient or *Mir155*-deficient GC-B cells were sorted 7 days after HEL$^{3\times}$-SRBC immunization. Libraries were prepared with Chromium Next GEM Single Cell 5' Reagent Kit v2 (10x Genomics) and sequenced on the Illumina NovaSeq 6000 platform. Fastq files were aligned and counted using CellRanger (v. 6.1.2) and using as reference mm10-2020-A (obtained from 10x Genomics). Matrices were imported into Seurat (v. 4.0.5) (*77*), which was sued for downstream analysis. After QC, cells with less than 1000 features and more than 10% mitochondrial content were removed. Data was then normalized, scaled and variable features were identified per cell. Samples were integrated using "CCA" by integrating in the following order, first all replicates for each genotype and then by genotypes. DoubletFinder (*78*) was used to predict doublets. Clusters identified as contaminating for expression of *Cd8a, Cd3e, Cd3d, Lyz2* and *Gzma,* and cells labelled as doublets were removed from the analysis. Clusters were manually annotated using differential expressed genes obtained from FindMarkers. Uniform Manifold Approximation and Projection (UMAP) was used for visualization. VlnPlots and FeaturePlots have been used to display gene expression values per cluster or overlay on UMAP. The merged dataset of biological triplicates contained 25,358 and 24,087 GC-B cells for WT and KO cells, respectively. Unsupervised clustering using Seurat (*77*) identified nine distinct clusters, each with their unique cell cycle status determined by the expression of genes associated with different phases of the cell cycle (***Supplemental Figure 1E*** and ***1F***). For gene signatures, a score was calculated using AddModuleScore prior to plotting. Statistical significance was obtained using Wilcoxon test and multiple comparison correction was performed using the "fdr" procedure. Differential gene expression between genotypes per cluster was carried out using a pseudobulk approach, in which gene counts were aggregated per sample and the "pseudoBulkDGE" function from the scran package (*79*) was used with the design ~genotype. Genes are considered differentially expressed if FDR < 0.05. For trajectory analysis, Partition-based graph abstraction PAGA (*32*) was used. The integrated Seurat object was converted into a h5 format, neighbors were computed using 20 pcs and clusters detected using Seurat were used to compute the paga graph. Mitochondrial gene list was downloaded from MitoCarta3.0 (*55*).

ChIP-seq and data analysis

WT and KO B cells were cultured under hypoxic conditions with positive selection mimicking stimulants for 2 days. Cells were fixed for 1 hr in 2 mM EGS, followed by 15 min in 1% Formaldehyde. Chromatin was sheared using Bioruptor Pico sonication device (Diagenode). An aliquot of the chromatin was used to assess the size of the DNA fragments obtained by High

Sensitivity NGS Fragment Analysis Kit (Agilent) on Fragment Analyzer (Agilent). ChIP was performed using IP-Star Compact Automated System (Diagenode). Chromatin corresponding to 13.5 µg and 1 µg were immunoprecipitated with KDM2A antibody (a gift from R. Klose, University of Oxford) and H3K36me2 (Abcam). Chromatin corresponding to 1% was used as Input. Libraries were prepared using MicroPlex Library Preparation Kit v3 (Diagenode) with 24 UDI for MicroPlex v3 (Diagenode). Generated libraries were purified using Agencourt AMPure XP (Beckman Coulter) and quantified using Qubit dsDNA HS Assay Kit (ThermoFisher Scientific). The fragment size was analyzed by High Sensitivity NGS Fragment Analysis Kit on Fragment Analyzer. Sequencing was carried out on the Illumina NovaSeq 6000 platform. Read alignment, library QC, peak detection and quantification was carried out using the nf-core/chipseq pipeline (v. 1.2.2), using "-profile crick --min_reps_consensus 2". Briefly, reads were aligned using BWA (*80*) to GRCm38 using the genomes provided with the pipeline. Peaks were called using MACS2 (*81*) and annotated using HOMER (*82*). A list of consensus peaks is generated as the union of peaks detected in at least two replicates per condition. Bigwigs generated by the pipeline (scaled to 1 million mapped reads) were used to generate meta profile plots with Deeptools "compute matrix" (*83*). A table containing CpG island containing genes was obtained from UCSC Table Browser (*84*). Initially, an average of 26436 and 17586 KDM2A peaks were identified for WT and KO cells, respectively. The peaks that only one of the triplicate samples bound were removed from the subsequent analysis. After the exclusion of peaks, there were 9129 KDM2A peaks that were bound by both WT and KO B cells. The average fold change (fc) was calculated by dividing the average KDM2A peak signal by the input signal, and then "WT-enriched" or "KO-enriched" peaks among the 9129 KDM2A peaks bound by both WT and KO B cells were determined based on a fold change threshold (fc >3) and a ratio of average fc between WT and KO cells (>$2^{0.23}$-fold enrichment). Peaks with an fc >3 from "peaks bound only by WT" (5905) and "peaks bound only by KO" (1479) were also categorized as "WT-enriched" and "KO-enriched" KDM2A peaks, respectively. After applying the selection threshold, a total of 1403 genes with 1453 "WT-enriched KDM2A" peaks and 309 genes with 309 "KO-enriched KDM2A" peaks were identified (***Supplemental Table 3***). Among these, 73.6% and 78.0% of the "WT-enriched KDM2A" peaks and "KO-enriched KDM2A" peaks, respectively are genes containing CpG island.

Statistical analysis

Statistical significance was determined by unpaired, two-tailed Student's t-test, Kruskal-Wallis one-way analysis of variance (ANOVA) with multiple comparisons, or Wilcoxon rank sum test. The statistical method used is indicated in the respective figure legends. Prism 9 (v.9.4.1) software (GraphPad) and R (v.4.2.0) were used to calculate all statistical analyses.

Data availability

The scRNA-seq, bulk RNA-seq and ChIP-seq data have been deposited in the NCBU Gene Expression Omnibus (GEO) database under accession number GSE230528, GSE231649, GSE230527, respectively. Source data are provided with this paper.

Code availability

Code used in this study is available at Github: https://github.com/djpbarry/MitoRosQuant

Acknowledgements
We thank M. Busslinger (Research Institute of Molecular Pathology) for *Aicda-cre*-h*CD2* mice; B. P. Sleckman (University of Alabama at Birmingham) for *Myc*$^{gfp/gfp}$ mice; R. Brink (Garvan Institute of Medical Research/University of New South Wales) for SW_{HEL} mice; O. Bannard (University of Oxford) for providing CHO-his-tagged $HEL^{3\times}$ cells; the staff of Genomics Facility of the Babraham Institute for technical support; the staff of the Francis Crick Institute Animal Facility, the Flow Cytometry Facility, the Advanced Sequencing Facility, the Advanced Light Microscopy Facility, and the Experimental Histopathology Facility for technical support; and E. Vigorito and C. Vinuesa for critical review.

Funding
This work was supported by the Francis Crick Institute which receives core funding from Cancer Research UK Grants (grant CC2078), the UK Medical Research Council Grants (grant CC2078), and Wellcome Trust Grants (grant CC2078) to D.P.C., BBSRC (BBS/E/B/000C0407) to M.T., and the National Institute of General Medical Sciences of the National Institutes of Health (P41 GM108569) to N.L.K.

Author contributions
R.N. conceived and designed the study. M.L. and P.C performed bioinformatic analysis. S.V-B. and G.D. generated *Kdm2a* mutant mice. R.N., J.M.C. and R.G. performed experiments and analyzed data. D.B. generated computational image analysis pipelines. N.P.B. and R.K. provided resources. N.L.K. provided supervision. M.T. interpreted data and critically revised the manuscript. R.N., and D.P.C. wrote the manuscript. All authors reviewed and edited the written manuscript.

Competing interests
The authors declare no direct competing financial or nonfinancial interests.

References

1. C. Berek, A. Berger, M. Apel, Maturation of the immune response in germinal centers. *Cell* **67**, 1121-1129 (1991).
2. J. Jacob, G. Kelsoe, K. Rajewsky, U. Weiss, Intraclonal generation of antibody mutants in germinal centres. *Nature* **354**, 389-392 (1991).
3. T. B. Kepler, A. S. Perelson, Cyclic re-entry of germinal center B cells and the efficiency of affinity maturation. *Immunol Today* **14**, 412-415 (1993).
4. R. Nakagawa, D. P. Calado, Positive Selection in the Light Zone of Germinal Centers. *Front Immunol* **12**, 661678 (2021).
5. D. P. Calado *et al.*, The cell-cycle regulator c-Myc is essential for the formation and maintenance of germinal centers. *Nat Immunol* **13**, 1092-1100 (2012).
6. D. Dominguez-Sola *et al.*, The proto-oncogene MYC is required for selection in the germinal center and cyclic reentry. *Nat Immunol* **13**, 1083-1091 (2012).
7. R. Nakagawa *et al.*, Permissive selection followed by affinity-based proliferation of GC light zone B cells dictates cell fate and ensures clonal breadth. *Proc Natl Acad Sci U S A* **118**, (2021).
8. F. J. Weisel *et al.*, Germinal center B cells selectively oxidize fatty acids for energy while conducting minimal glycolysis. *Nat Immunol* **21**, 331-342 (2020).
9. D. Chen *et al.*, Coupled analysis of transcriptome and BCR mutations reveals role of OXPHOS in affinity maturation. *Nat Immunol* **22**, 904-913 (2021).
10. J. Jellusova *et al.*, Gsk3 is a metabolic checkpoint regulator in B cells. *Nat Immunol* **18**, 303-312 (2017).
11. S. H. Cho *et al.*, Germinal centre hypoxia and regulation of antibody qualities by a hypoxia response system. *Nature* **537**, 234-238 (2016).
12. L. Li *et al.*, Regulation of humoral immune response by HIF-1alpha-dependent metabolic reprogramming of the germinal center reaction. *Cell Immunol* **367**, 104409 (2021).
13. S. J. Kierans, C. T. Taylor, Regulation of glycolysis by the hypoxia-inducible factor (HIF): implications for cellular physiology. *J Physiol* **599**, 23-37 (2021).
14. N. Goda *et al.*, Hypoxia-inducible factor 1alpha is essential for cell cycle arrest during hypoxia. *Mol Cell Biol* **23**, 359-369 (2003).
15. M. Koshiji *et al.*, HIF-1alpha induces cell cycle arrest by functionally counteracting Myc. *EMBO J* **23**, 1949-1956 (2004).
16. L. Liu *et al.*, Hypoxia-induced energy stress regulates mRNA translation and cell growth. *Mol Cell* **21**, 521-531 (2006).
17. J. Ersching *et al.*, Germinal Center Selection and Affinity Maturation Require Dynamic Regulation of mTORC1 Kinase. *Immunity* **46**, 1045-1058 e1046 (2017).
18. S. Finkin, H. Hartweger, T. Y. Oliveira, E. E. Kara, M. C. Nussenzweig, Protein Amounts of the MYC Transcription Factor Determine Germinal Center B Cell Division Capacity. *Immunity* **51**, 324-336 e325 (2019).
19. C. T. Mayer *et al.*, The microanatomic segregation of selection by apoptosis in the germinal center. *Science* **358**, (2017).
20. Y. Tsukada *et al.*, Histone demethylation by a family of JmjC domain-containing proteins. *Nature* **439**, 811-816 (2006).
21. Y. Tanaka *et al.*, JmjC enzyme KDM2A is a regulator of rRNA transcription in response to starvation. *EMBO J* **29**, 1510-1522 (2010).
22. E. Kawakami, A. Tokunaga, M. Ozawa, R. Sakamoto, N. Yoshida, The histone demethylase Fbxl11/Kdm2a plays an essential role in embryonic development by repressing cell-cycle regulators. *Mech Dev* **135**, 31-42 (2015).

23. L. Liu, J. Liu, Q. Lin, Histone demethylase KDM2A: Biological functions and clinical values (Review). *Exp Ther Med* **22**, 723 (2021).
24. L. A. Esposito, S. Melov, A. Panov, B. A. Cottrell, D. C. Wallace, Mitochondrial disease in mouse results in increased oxidative stress. *Proc Natl Acad Sci U S A* **96**, 4820-4825 (1999).
25. M. Redza-Dutordoir, D. A. Averill-Bates, Activation of apoptosis signalling pathways by reactive oxygen species. *Biochim Biophys Acta* **1863**, 2977-2992 (2016).
26. R. Nakagawa *et al.*, MicroRNA-155 controls affinity-based selection by protecting c-MYC+ B cells from apoptosis. *J Clin Invest* **126**, 377-388 (2016).
27. T. G. Phan *et al.*, B cell receptor-independent stimuli trigger immunoglobulin (Ig) class switch recombination and production of IgG autoantibodies by anergic self-reactive B cells. *J Exp Med* **197**, 845-860 (2003).
28. C. Y. Huang, A. L. Bredemeyer, L. M. Walker, C. H. Bassing, B. P. Sleckman, Dynamic regulation of c-Myc proto-oncogene expression during lymphocyte development revealed by a GFP-c-Myc knock-in mouse. *Eur J Immunol* **38**, 342-349 (2008).
29. K. Kwon *et al.*, Instructive role of the transcription factor E2A in early B lymphopoiesis and germinal center B cell development. *Immunity* **28**, 751-762 (2008).
30. B. J. Laidlaw, L. Duan, Y. Xu, S. E. Vazquez, J. G. Cyster, The transcription factor Hhex cooperates with the corepressor Tle3 to promote memory B cell development. *Nat Immunol* **21**, 1082-1093 (2020).
31. D. Suan *et al.*, CCR6 Defines Memory B Cell Precursors in Mouse and Human Germinal Centers, Revealing Light-Zone Location and Predominant Low Antigen Affinity. *Immunity* **47**, 1142-1153 e1144 (2017).
32. F. A. Wolf *et al.*, PAGA: graph abstraction reconciles clustering with trajectory inference through a topology preserving map of single cells. *Genome Biol* **20**, 59 (2019).
33. S. Mroczek, J. Kufel, Apoptotic signals induce specific degradation of ribosomal RNA in yeast. *Nucleic Acids Res* **36**, 2874-2888 (2008).
34. A. Toboso-Navasa *et al.*, Restriction of memory B cell differentiation at the germinal center B cell positive selection stage. *J Exp Med* **217**, (2020).
35. G. Huang, H. Li, H. Zhang, Abnormal Expression of Mitochondrial Ribosomal Proteins and Their Encoding Genes with Cell Apoptosis and Diseases. *Int J Mol Sci* **21**, (2020).
36. J. M. Camarillo *et al.*, Coupling Fluorescence-Activated Cell Sorting and Targeted Analysis of Histone Modification Profiles in Primary Human Leukocytes. *J Am Soc Mass Spectrom* **30**, 2526-2534 (2019).
37. B. A. Garcia *et al.*, Chemical derivatization of histones for facilitated analysis by mass spectrometry. *Nat Protoc* **2**, 933-938 (2007).
38. Y. Zhao, B. A. Garcia, Comprehensive Catalog of Currently Documented Histone Modifications. *Cold Spring Harb Perspect Biol* **7**, a025064 (2015).
39. B. J. Klein *et al.*, Histone H3K23-specific acetylation by MORF is coupled to H3K14 acylation. *Nat Commun* **10**, 4724 (2019).
40. H. Chen *et al.*, H3K36 dimethylation shapes the epigenetic interaction landscape by directing repressive chromatin modifications in embryonic stem cells. *Genome Res* **32**, 825-837 (2022).
41. X. Tian *et al.*, Histone lysine-specific methyltransferases and demethylases in carcinogenesis: new targets for cancer therapy and prevention. *Curr Cancer Drug Targets* **13**, 558-579 (2013).
42. M. Batie, J. Druker, L. D'Ignazio, S. Rocha, KDM2 Family Members are Regulated by HIF-1 in Hypoxia. *Cells* **6**, (2017).

43. X. Xia *et al.*, Integrative analysis of HIF binding and transactivation reveals its role in maintaining histone methylation homeostasis. *Proc Natl Acad Sci U S A* **106**, 4260-4265 (2009).
44. R. K. Abbott *et al.*, Germinal Center Hypoxia Potentiates Immunoglobulin Class Switch Recombination. *J Immunol* **197**, 4014-4020 (2016).
45. M. Zaidi, F. Fu, D. Cojocari, T. D. McKee, B. G. Wouters, Quantitative Visualization of Hypoxia and Proliferation Gradients Within Histological Tissue Sections. *Front Bioeng Biotechnol* **7**, 397 (2019).
46. U. Bruning *et al.*, MicroRNA-155 promotes resolution of hypoxia-inducible factor 1alpha activity during prolonged hypoxia. *Mol Cell Biol* **31**, 4087-4096 (2011).
47. G. Wan *et al.*, Hypoxia-induced MIR155 is a potent autophagy inducer by targeting multiple players in the MTOR pathway. *Autophagy* **10**, 70-79 (2014).
48. H. Y. Cho, E. Loreti, M. C. Shih, P. Perata, Energy and sugar signaling during hypoxia. *New Phytol* **229**, 57-63 (2021).
49. I. Papandreou, R. A. Cairns, L. Fontana, A. L. Lim, N. C. Denko, HIF-1 mediates adaptation to hypoxia by actively downregulating mitochondrial oxygen consumption. *Cell Metab* **3**, 187-197 (2006).
50. H. G. Crabtree, Observations on the carbohydrate metabolism of tumours. *Biochem J* **23**, 536-545 (1929).
51. S. Rodriguez-Enriquez, O. Juarez, J. S. Rodriguez-Zavala, R. Moreno-Sanchez, Multisite control of the Crabtree effect in ascites hepatoma cells. *Eur J Biochem* **268**, 2512-2519 (2001).
52. L. D. Marroquin, J. Hynes, J. A. Dykens, J. D. Jamieson, Y. Will, Circumventing the Crabtree effect: replacing media glucose with galactose increases susceptibility of HepG2 cells to mitochondrial toxicants. *Toxicol Sci* **97**, 539-547 (2007).
53. N. P. Blackledge *et al.*, CpG islands recruit a histone H3 lysine 36 demethylase. *Mol Cell* **38**, 179-190 (2010).
54. W. Huang da, B. T. Sherman, R. A. Lempicki, Systematic and integrative analysis of large gene lists using DAVID bioinformatics resources. *Nat Protoc* **4**, 44-57 (2009).
55. S. Rath *et al.*, MitoCarta3.0: an updated mitochondrial proteome now with sub-organelle localization and pathway annotations. *Nucleic Acids Res* **49**, D1541-D1547 (2021).
56. D. Kitamura, J. Roes, R. Kuhn, K. Rajewsky, A B cell-deficient mouse by targeted disruption of the membrane exon of the immunoglobulin mu chain gene. *Nature* **350**, 423-426 (1991).
57. A. Rodriguez *et al.*, Requirement of bic/microRNA-155 for normal immune function. *Science* **316**, 608-611 (2007).
58. T. H. Thai *et al.*, Regulation of the germinal center response by microRNA-155. *Science* **316**, 604-608 (2007).
59. E. Vigorito *et al.*, microRNA-155 regulates the generation of immunoglobulin class-switched plasma cells. *Immunity* **27**, 847-859 (2007).
60. J. P. Hsin, Y. Lu, G. B. Loeb, C. S. Leslie, A. Y. Rudensky, The effect of cellular context on miR-155-mediated gene regulation in four major immune cell types. *Nat Immunol* **19**, 1137-1145 (2018).
61. D. Pasini *et al.*, JARID2 regulates binding of the Polycomb repressive complex 2 to target genes in ES cells. *Nature* **464**, 306-310 (2010).
62. C. Schneider *et al.*, FBXO11 inactivation leads to abnormal germinal-center formation and lymphoproliferative disease. *Blood* **128**, 660-666 (2016).
63. D. Paus *et al.*, Antigen recognition strength regulates the choice between extrafollicular plasma cell and germinal center B cell differentiation. *J Exp Med* **203**, 1081-1091 (2006).

64. Z. Long, B. Phillips, D. Radtke, M. Meyer-Hermann, O. Bannard, Competition for refueling rather than cyclic reentry initiation evident in germinal centers. *Sci Immunol* **7**, eabm0775 (2022).
65. W. Piao *et al.*, Development of azo-based fluorescent probes to detect different levels of hypoxia. *Angew Chem Int Ed Engl* **52**, 13028-13032 (2013).
66. D. R. Stirling *et al.*, CellProfiler 4: improvements in speed, utility and usability. *BMC Bioinformatics* **22**, 433 (2021).
67. J. Schindelin *et al.*, Fiji: an open-source platform for biological-image analysis. *Nat Methods* **9**, 676-682 (2012).
68. D. Legland, I. Arganda-Carreras, P. Andrey, MorphoLibJ: integrated library and plugins for mathematical morphology with ImageJ. *Bioinformatics* **32**, 3532-3534 (2016).
69. B. Li, C. N. Dewey, RSEM: accurate transcript quantification from RNA-Seq data with or without a reference genome. *BMC Bioinformatics* **12**, 323 (2011).
70. B. Langmead, S. L. Salzberg, Fast gapped-read alignment with Bowtie 2. *Nat Methods* **9**, 357-359 (2012).
71. M. I. Love, W. Huber, S. Anders, Moderated estimation of fold change and dispersion for RNA-seq data with DESeq2. *Genome Biol* **15**, 550 (2014).
72. A. Subramanian *et al.*, Gene set enrichment analysis: a knowledge-based approach for interpreting genome-wide expression profiles. *Proc Natl Acad Sci U S A* **102**, 15545-15550 (2005).
73. D. Merico, R. Isserlin, O. Stueker, A. Emili, G. D. Bader, Enrichment map: a network-based method for gene-set enrichment visualization and interpretation. *PLoS One* **5**, e13984 (2010).
74. Y. Chen, X. Wang, miRDB: an online database for prediction of functional microRNA targets. *Nucleic Acids Res* **48**, D127-D131 (2020).
75. I. S. Vlachos *et al.*, DIANA-TarBase v7.0: indexing more than half a million experimentally supported miRNA:mRNA interactions. *Nucleic Acids Res* **43**, D153-159 (2015).
76. V. Agarwal, G. W. Bell, J. W. Nam, D. P. Bartel, Predicting effective microRNA target sites in mammalian mRNAs. *Elife* **4**, (2015).
77. R. Satija, J. A. Farrell, D. Gennert, A. F. Schier, A. Regev, Spatial reconstruction of single-cell gene expression data. *Nat Biotechnol* **33**, 495-502 (2015).
78. C. S. McGinnis, L. M. Murrow, Z. J. Gartner, DoubletFinder: Doublet Detection in Single-Cell RNA Sequencing Data Using Artificial Nearest Neighbors. *Cell Syst* **8**, 329-337 e324 (2019).
79. A. T. Lun, D. J. McCarthy, J. C. Marioni, A step-by-step workflow for low-level analysis of single-cell RNA-seq data with Bioconductor. *F1000Res* **5**, 2122 (2016).
80. H. Li, R. Durbin, Fast and accurate short read alignment with Burrows-Wheeler transform. *Bioinformatics* **25**, 1754-1760 (2009).
81. Y. Zhang *et al.*, Model-based analysis of ChIP-Seq (MACS). *Genome Biol* **9**, R137 (2008).
82. S. Heinz *et al.*, Simple combinations of lineage-determining transcription factors prime cis-regulatory elements required for macrophage and B cell identities. *Mol Cell* **38**, 576-589 (2010).
83. F. Ramirez *et al.*, deepTools2: a next generation web server for deep-sequencing data analysis. *Nucleic Acids Res* **44**, W160-165 (2016).
84. D. Karolchik *et al.*, The UCSC Table Browser data retrieval tool. *Nucleic Acids Res* **32**, D493-496 (2004).

Figure legends

Figure 1. MiR-155 is required for promoting mitochondrial fitness in GC-B cells.
(A) Experimental design for all the experiments for Figure 1. (B) Percentage of MitoSOX^{+} cells or active-Caspase 3^{+} GC-B cells at 5 days or 7 days after HEL$^{3\times}$-SRBC immunization, respectively. Statistical analysis was performed using Student's *t*-test. *P<0.05, **p<0.01, *** p<0.001, ****p<0.0001. (C) The PAGA algorithm generates a topology-preserving map of single cells along with the sequential changes of gene expression. PAGA graphs were constructed using a k-nearest neighbors' algorithm to show relationships between clusters. The Ball-and-stick representation displays PAGA connectivity among GC-B cell clusters identified though scRNA-seq. Ball size represents cluster size, and edge thickness indicates connectivity between clusters. Normalized gene expression for *Cxcr4* or *Myc* is shown in the PAGA graph. (D) Predicted relationship between the clusters identified in scRNA-seq of GC-B cells. (E) Violin plots showing gene signature scores for "Mitochondrion" and "OXPHOS". Statistical analysis was performed using Wilcoxon rank sum test, *p<0.05, ****p<0.00005, n.s., not significant. (F) Enrichment map visualizing GSEA results of bulk RNA-seq data from WT and KO cMyc^{+} LZ GC-B cells. GC-B cells were sorted 5 days after HEL$^{3\times}$-SRBC immunization. WT-enriched pathways (q<0.0001) were used. Nodes represent gene sets, and edges represent mutual overlap. Highly redundant gene sets were grouped as clusters. GSEA enrichment plots for "OXPHOS" and "Mitochondrial translation" are shown. ES; enriched score, FDR; false discovery rate. Pooled data from more than two experiments with 12 mice each for WT and KO mice in MitoSOX staining, and 18 and 19 mice for WT and KO mice, respectively, in active-Caspase3 staining (B).

Figure 2. MiR-155 regulates H3K36me2 levels in dividing LZ GC-B cells.
(A) Enrichment map visualizing GSEA results of bulk RNA-seq data from WT and KO cMyc$^+$ LZ GC-B cells. KO-enriched pathways (q<0.1) were used. (B) The relative abundance of histone PTMs, including histone H3.1 K36, H3.3 K36, H3.1 K27 and H3.3 K27 in LZ GC-B cells from WT and KO mice. Donor-derived GC-B cells (GC-B cell gating: CD45.1$^-$ CD45.2$^+$ B220$^+$ HEL$^+$ CD38^{lo} CD95$^+$) were sorted 5 days after adoptive transfer for analysis. Statistical analysis was performed with Student's *t*-test. **p<0.01, n.s., not significant. (C) Splenic sections of C57BL/6 mice, in the presence and absence of miR-155 seven days after SRBC immunization were stained for GL7 (green), MYC (red) and H3K36me2 (blue). Yellow wedges represent cells that are positive for MYC but negative for KDM2A. Scale bar, 50 µm. Representative images from two experiments with four mice each for WT and KO backgrounds. (D) Scatter plots show the mean intensity (MI) of MYC and H3K36me2 per segmented cell within GCs of spleen sections obtained from immunized WT and KO C57BL/6 mice. Cell segmentation within GCs was performed using DAPI staining on the sections. The Pearson's correlation coefficient indicates the co-expression relationship between MYC and H3K36me2, with the corresponding coefficient value (r) and a 95% confidence interval displayed. (E) Relative H3K36me2 levels determined by calculating the ratio of H3K36me2 MI to MYC MI from (D). The top 5% of MYC intensity values, representing the highest MYC expressing cells, were selected from each batch of imaging experiments. Statistical analysis was performed using Student's *t*-test. ****p<0.0001.

Figure 3. MiR-155 primarily controls KDM2A expression in high affinity cMyc$^+$ LZ GC-B cells.

(A) Heat map showing the transcript levels of the enzymes involved in the demethylation of histone H3K36me2. The bulk RNA-seq dataset from WT and KO cMyc$^+$ LZ GC-B cells was used. FDR values are shown. n.s., not significant. (B) Sequence alignment of a part of the 3'UTR of *Kdm2a*. The 8-mer miR-155 binding site is highlighted in a box. (C) Immunofluorescence staining of splenic section from a WT mouse 7 days after SRBC immunization, showing IgD (white), MYC (red) and KDM2A (blue). Scale bar, 50 µm. Representative section image from two experiments with four mice each for WT and KO backgrounds. (D) Scatter plots show the MI of MYC and KDM2A within segmented GC cells in spleen sections from immunized WT and KO mice. The Pearson's correlation coefficient (r) is presented with a 95% confidence interval. (E) Relative MFI of KDM2A in cells from four GC-B cell subpopulations. GC-B cells were derived from WT or KO donor B cells 7 days after HEL$^{3\times}$-SRBC immunization. Each dot represents one mouse. (F) Relative MFI of KDM2A in cells from four GC-B cell subpopulations. GC-B cells were derived from WT or KO donor B cells 7 days after HEL$^{3\times}$-SRBC immunization. Low and high affinity were determined based on HEL$^{3\times}$ binding within Igκ$^+$ GC-B cells. Pooled data from three experiments with 11 and 9 mice for WT and KO mice, respectively (E and F). Statistical analysis was performed using Student's *t*-test. *P<0.05, **p<0.01, *** p<0.001. n.s., not significant.

Figure 4. The regulatory activity of miR-155 is revealed under hypoxia.
(A) Representative flow cytometric histograms of hypoxia dye, MAR vs. relative cell number (RCN) (left). Relative MFI of MAR (right) in GC-B and non-GC-B cells. GC-B and non-GC-B cells were isolated from inguinal lymph nodes of C57BL/6 mice. Non-GC-B cells were gated as $CD19^+$ $B220^+$ $CD38^+$ $CD138^-$ $CD95^-$ $GL7^-$. (B) KDM2A MFI of B cells from WT and KO C57BL/6 mice cultured under normoxia (21% O_2) or hypoxia (1% O_2) for the indicated time periods. Each dot represents data from one mouse. (C) Representative flow cytometric histograms of CTV vs. RCN (top). CTV MFI of B cells from WT and KO C57BL/6 mice cultured under normoxia or hypoxia for the indicated time periods (bottom). Each dot represents data from one mouse. (D) Representative image of B cells from WT and KO C57BL/6 mice cultured under normoxia or hypoxia for 2 days, followed by staining with MitoTracker Deep Red (Red) and MitoTracker Orange CM-H_2 TMRos (green). DAPI (blue) was used as a nuclear counterstaining. Scale bar, 10 µm. Representative image from two independent experiments with four mice each for WT and KO backgrounds. (E) Quantification of relative MitoTracker Orange CMTMRos levels. Each dot represents one cell. (F) Relative ATP levels in B cells from WT and KO C57BL/6 mice. The replated cells were cultured for 2 hours in hypoxia with indicated media for ATP measurement. The luminescence values of each type of B cells cultured in media containing glucose for 2 hours in hypoxia were used to calculate relative ATP levels. Pooled data from more than two experiments with 6 WT mice (A), 5 mice each for WT and KO mice (B and C), 4 mice each for WT and KO mice (E), and 3 mice each for WT and KO mice (F). Statistical analysis was performed using Student's *t*-test (B and C) or one-way ANOVA (A, E and F). *P<0.05, **p<0.01, *** p<0.001, ****p<0.0001, n.s., not significant.

Figure 5. MiR-155 optimizes unclear mitochondrial gene expression through *Kdm2a*-mediated control of H3K36me2 levels.

(A) Genomic distribution of KDM2A and H3K36me2 ChIP-seq peaks in B cells from WT and KO mice cultured for 2 days in hypoxia is shown as pie charts. The average percentage of the ChIP-seq triplicate samples is displayed. Promoter regions are defined as ± 2 kb of the transcription start site (TSS). (B) Metagene analysis and heatmaps of KDM2A or H3K36me2 for CpG islands (CGIs) containing genes or genes without CGIs. Metagene analyses are displayed in ± 10 kb windows. A representative sample is shown. (C) Plots showing the distribution of peak distance to nearest TSS. The average ChIP-seq read occupancy for KDM2A or H3K36me2 surrounding the TSS of CGIs containing genes. (D) Analysis of genes with "WT-enriched" and "KO-enriched" KDM2A peaks using the DAVID Functional Annotation Clustering Tool. Pathways with a modified fisher exact p-value < 0.05 were included. (E) A heat map showing transcript levels of seven mitochondrial genes with "KO-enriched" KDM2A peaks at the promoter/TSS regions or first introns near the TSS. The bulk RNA-seq dataset of WT and KO cMyc^{+} LZ GC-B cells was used.

Figure 6. The miR-155-*Kdm2a* interaction regulates mitochondrial ROS and apoptosis in GC-B cells.

(A) Schematics representation of the 8-mer miR-155-binding site in the 3'UTR of the *Kdm2a* (boxed) and the introduced base changes (red letters) to disrupt miR-155 binding in *Kdm2a* mutant mice. (B) Representative flow cytometric histograms showing KDM2A vs. RCN. MFI is shown on the plot. Relative MFI of KDM2A in GC-B cells in the LZ or DZ. GC-B cells ($B220^{+}$ $CD38^{low}$ $CD95^{+}$ $GL7^{+}$) were derived from WT and MUT mice 7 days after SRBC immunization. (C) Number of LZ and DZ GC-B cells from WT and MUT mice within the μMT adoptive transfer system. (D) Representative flow cytometric plots of MitoTracker DeepRed vs. MitoSOX in GC-B cells from WT and MUT mice within the μMT adoptive transfer system. Percentage of $MitoSOX^{+}$ GC-B cells. (E) Representative flow cytometric plots of B220 vs. active-Caspase 3 in GC-B cells from WT and MUT mice within the μMT adoptive transfer system. Percentage of active-Caspase 3^{+} GC-B cells. Pooled data from two experiments with 4 mice each for WT and MUT C57BL/6 mice (B) and 7 mice each for WT and MUT mice (C, D and E). Statistical analysis was performed using Student's *t*-test (B, C, D and E). *P<0.05, **p<0.01, n.s., not significant.

Figure 7. Working model: miR-155-mediated epigenetic regulation during GC-B cell positive selection.

Following the reception of signals through BCR engagement and T cell help, LZ GC-B cells undergo a positive selection process that induces the expression of miR-155 and KDM2A. Moreover, KDM2A expression is synergistically induced in the hypoxic LZ microenvironment. Positively selected GC-B cells then migrate to the less hypoxic DZ and sustain their vigorous cell division by relying on OXPHOS for energy production. However, the transition from the LZ to the DZ presents a considerable challenge, as GC-B cells undergo substantial changes in gene expression profiles under hypoxia-induced stress. To facilitate this dynamic transition, miR-155 plays a crucial role by repressing the expression of KDM2A. This repression mechanism ensures precise regulation of H3K36me2 levels at the promoter/TSS regions of CpG-containing genes. As a result, optimal expression of nuclear mitochondrial genes is maintained, facilitating mitochondrial remodeling, and enhancing OXPHOS efficiency. The absence of miR-155 expression in positively selected GC-B cells results in increased levels of KDM2A expression, which disrupts H3K36me2 levels and leads to mitochondrial dysfunction, ultimately culminating in cell death.

Supplementary Figure 1. Gene expression patterns of miR-155-sufficient and miR-155-difficient GC-B cell clusters.

(A) Flow cytometry gating strategy for isolating splenic donor GC-B cells 7 days after HEL$^{3\times}$-SRBC immunization. (B) Schematics illustrating the relationship between four GC-B cell subpopulations (cMyc^{-} LZ, cMyc^{+} LZ, cMyc^{+} DZ and cMyc^{-} DZ) and the expression patterns of cMyc and miR-155. (C) MFI values of cMyc-GFP in GC-B cells from WT and KO, 8 days after HEL$^{3\times}$-SRBC immunization. (D) Quantification of cMyc^{+} LZ and DZ GC-B cell numbers in WT and KO mice, 5 days after HEL$^{3\times}$-SRBC immunization. (E) UMAP plots displaying merged scRNA-seq profiles from WT and KO GC-B cells, with 9 clusters (left) and predicted cell cycle phases (right). (F) UMAP plots showing scRNA-seq profiles from WT or KO GC-B cells, with 9 identified clusters. (G) UMAP plots colored by the normalized expression of signature genes associated with LZ, DZ and Myc signature genes. (H) Ball-and-stick representation of PAGA connectivity among scRNA-seq GC-B cell clusters from WT or KO GC-B cells. (I) UMAP plots colored by the number of genes detected in each cell or the percentage of mitochondrial genes. (J) Violin plots illustrating the expression levels of *Rps21* or *Rpl14* in the GC-B cell clusters. (K) Top 8 GSEA gene signatures in WT vs. KO comparison using RNA-seq dataset of cMyc^{+} LZ GC-B cells. WT-enriched gene signatures are shown. FDR; false discovery rate, NEM; normalized enrichment score. Pooled data from more than two experiments with 11 mice each for WT and KO mice (C), 13 and 14 mice for WT and KO mice, respectively (D). Statistical analysis was performed using Student's *t*-test (C and D), ****$p<0.0001$, n.s., not significant.

Supplementary Figure 2. Histone PTM states in *Mir155*-sufficient and *Mir155*-deficient GC-B cells.

(A) The relative abundance of histone PTMs in LZ GC-B cells from WT and KO mice. Donor-derived GC-B cells were sorted 5 days after adoptive transfer for the analysis. (B) The relative abundance of histone PTMs, including histone H3.1 K36, H3.3 K36, H3.1 K27 and H3.3 K27, in DZ GC-B cells from WT and KO mice. Donor-derived GC-B cells were sorted 5 days after adoptive transfer for the analysis. (C, D) Immunofluorescence staining of splenic sections from WT mice 7 days after SRBC immunization, showing IgD (white), MYC (red) and H3K36me1 (C) or H3K36me3 (D) (green). Scale bar, 20 μm. Scatter plots illustrating the expression of MYC and H3K36me1(C) or H3K36me3 (D) in segmented GC cells within spleen sections from immunized WT and KO mice. Pearson's correlation coefficient (r) indicates the co-expression between MYC and H3K36me1 (C) or H3K36me3 (D).

Supplementary Figure 3. The histone demethylase *Kdm2a* is a target of miR-155.
(A) Heat map showing the transcript levels of the miR-155 targets. The miR-155 targets displaying a significant (FDR <0.05) and at least 1.3-fold increase in KO cMyc$^+$ LZ GC-B cells compared to WT are shown. The bulk RNA-seq dataset of WT and KO cMyc$^+$ LZ GC-B cells was used. (B) Representative flow cytometric histograms showing KDM2A vs. relative cell number (RCN).

Supplementary Figure 4. Induction of miR-155 by positive selection signals in normoxia and hypoxia.

(A) MiR-155 expression levels in B cells cultured under normoxia and hypoxia. Each dot represents one mouse sample. (B) Relative luminescence units (RLU) of B cells cultured in glucose containing media for 2 hours in hypoxia. Pooled data from three experiments with 3 mice each for WT and KO mice. Statistical analysis was performed using Student's *t*-test (A) or one-way ANOVA (B). *$p<0.05$, **$p<0.01$, ****$p<0.0001$, n.s., not significant.

Supplementary Figure 5. Increased KDM2A expression exacerbates mitochondrial ROS in the absence of miR-155.

(A) Total B lineage cell numbers in the spleen of WT and MUT mice. T1: $CD19^+$ $B220^+$ $AA4.1^+$ $CD23^-$ IgM^+; T2: $CD19^+$ $B220^+$ $AA4.1^+$ $CD23^+$ IgM^+; T3: $CD19^+$ $B220^+$ $AA4.1^+$ $CD23^+$ IgM^{low}; Follicular (Fo) B: $CD19^+$ $B220^+$ $AA4.1^-$ $CD23^+$ IgM^{low}; Marginal zone (MZ) B: $CD19^+$ $B220^+$ $AA4.1^-$ $CD23^{low}$ IgM^+. (B) Representative flow cytometric plots showing the analysis of μMT mice transferred with or without donor B cells from a WT mouse 6 days after SRBC immunization. Recipient μMT mice without donor B cells failed to generate GC-B cells. (C) Representative flow cytometric plots analyzing μMT mice transferred with WT or MUT B cells 7 days after SRBC immunization. (D) Activated SW_{HEL} B cells were transduced with *Kdm2a* or control (empty) lentivirus. MFI of KDM2A was analyzed in activated B cells cultured for two days following transduction. GC-B cells derived from transduced donor cells were stained for MitoSOX 4 days after $HEL^{3\times}$-SRBC immunization (right). Pooled data from two experiments with 4 mice each for WT and MUT C57BL/6 mice (A) and 10 mice each for control-transduced and *Kdm2a*-transduced mice (D). Statistical analysis was performed using Student's *t*-test (A and D). **$p<0.01$, n.s., not significant.

Supplementary Table 1. Cluster marker genes in scRNA-seq of WT and KO GC-B cells.

Supplementary Table 2. Differentially expressed genes in bulk RNA-seq of WT and KO cMyc^{+} LZ GC-B cells.

Supplementary Table 3. WT- and KO-enriched KDM2A peaks in activated B cells.

Supplementary Table 4. Antibody list.

Fig.1

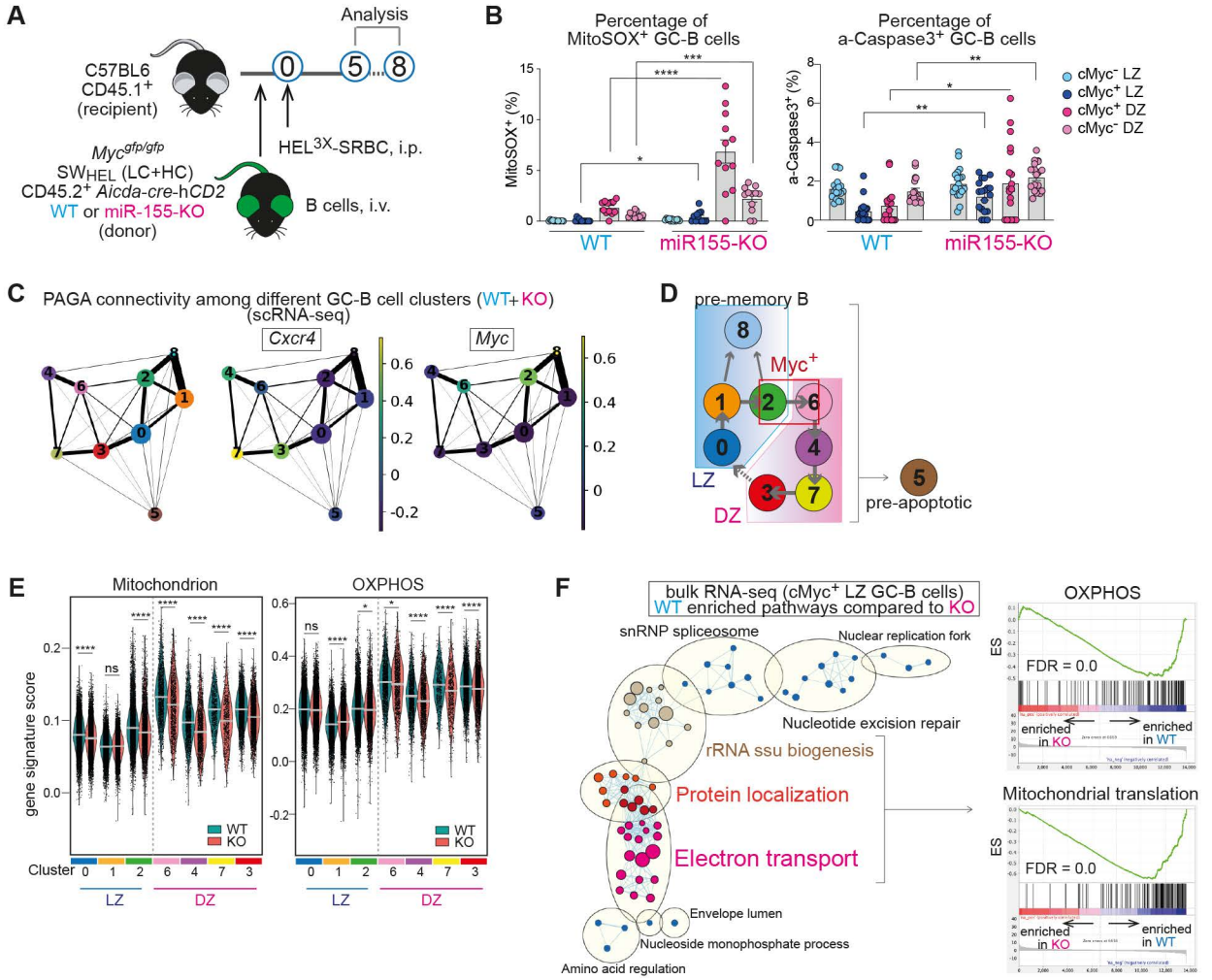
A
Analysis
C57BL6
CD45.1+
(recipient)
0
5
8
HEL3X-SRBC, i.p.
Mycgfp/gfp
SWHEL (LC+HC)
CD45.2+ Aicda-cre-hCD2
WT or miR-155-KO
(donor)
B cells, i.v.
B
Percentage of MitoSOX+ GC-B cells
MitoSOX+ (%)
WT
miR155-KO
Percentage of a-Caspase3+ GC-B cells
a-Caspase3+ (%)
cMyc- LZ
cMyc+ LZ
cMyc+ DZ
cMyc- DZ
C
PAGA connectivity among different GC-B cell clusters (WT+ KO)
(scRNA-seq)
Cxcr4
Myc
D
pre-memory B
Myc+
LZ
DZ
pre-apoptotic
E
Mitochondrion
OXPHOS
gene signature score
WT
KO
Cluster
LZ
DZ
F
bulk RNA-seq (cMyc+ LZ GC-B cells)
WT enriched pathways compared to KO
snRNP spliceosome
Nuclear replication fork
Nucleotide excision repair
rRNA ssu biogenesis
Protein localization
Electron transport
Envelope lumen
Nucleoside monophosphate process
Amino acid regulation
OXPHOS
FDR = 0.0
enriched in KO
enriched in WT
Mitochondrial translation
ES

Fig.2

A

bulk RNA-seq (cMyc+ LZ GC-B cells)
KO enriched pathwas compared to WT

Demethylation

Pathway	NES	FDR
GO_Histone demethylase activity	2.40	0.007
GO_Protein demethylation	2.39	0.005
GO_Demethylase activity	2.33	0.007
GO_Demethylation	2.23	0.040

B

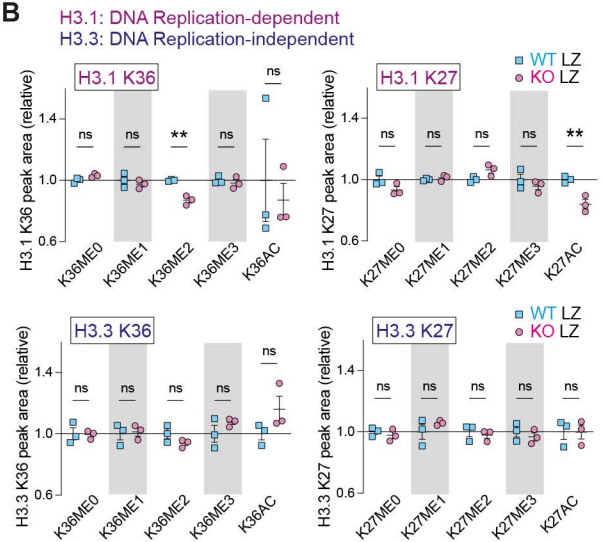

C

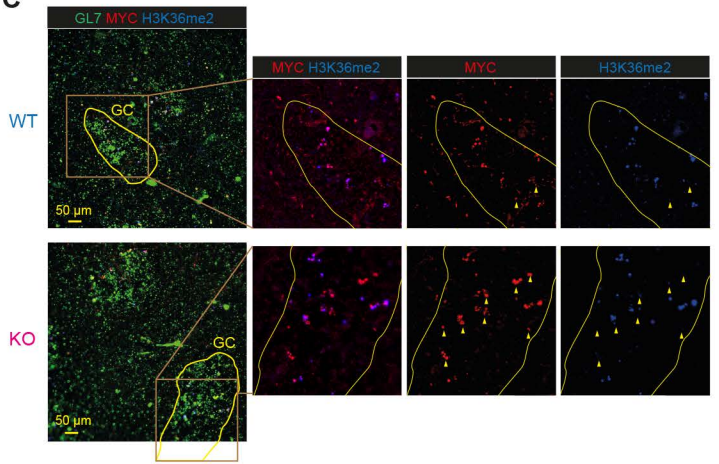

D

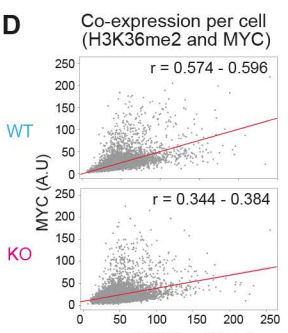

E

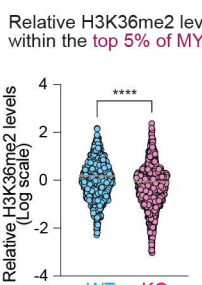

Fig. 3

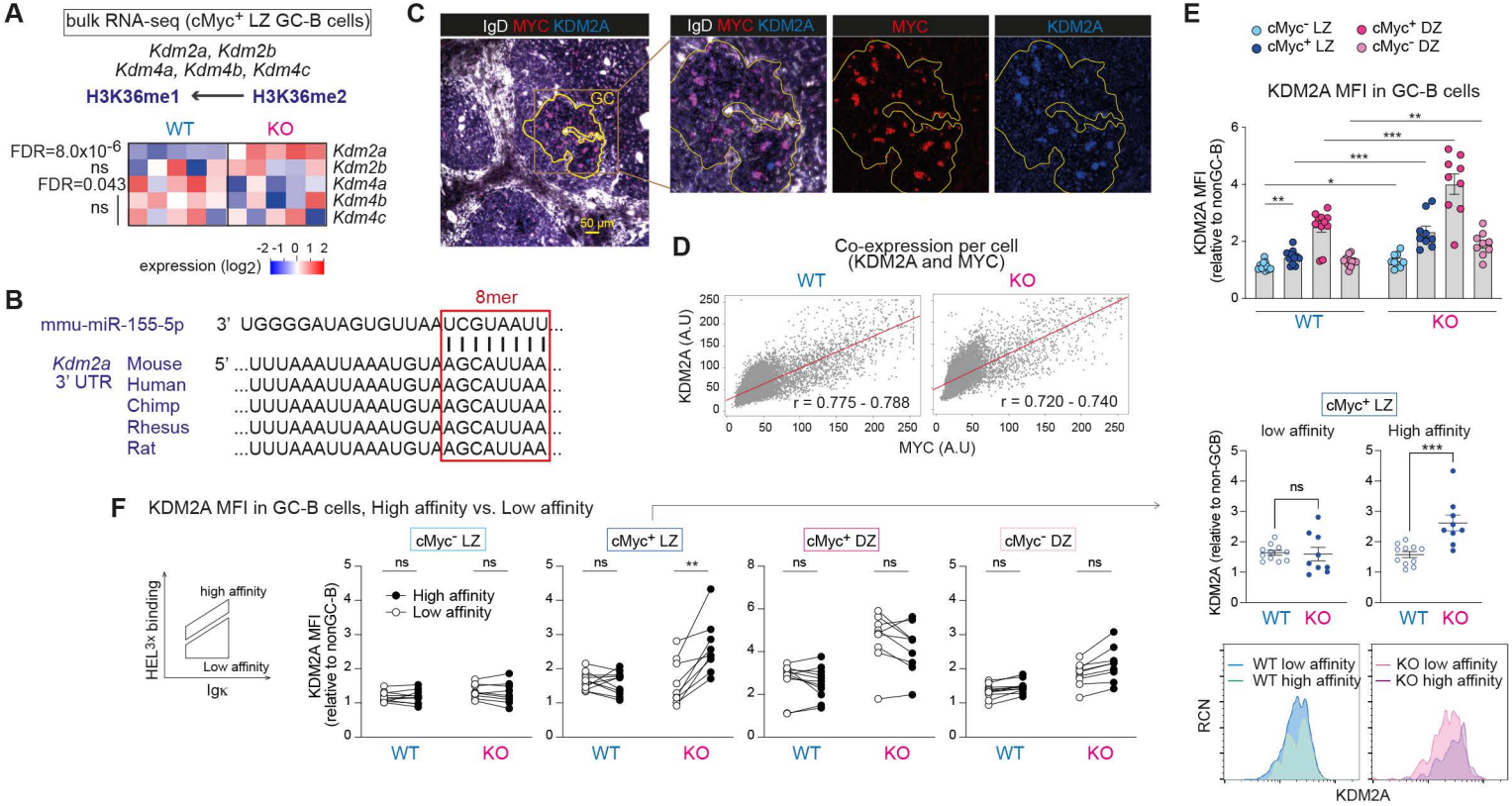
A
bulk RNA-seq (cMyc+ LZ GC-B cells)
Kdm2a, Kdm2b
Kdm4a, Kdm4b, Kdm4c
H3K36me1 ← H3K36me2
WT
KO
FDR=8.0x10-6
ns
FDR=0.043
ns
Kdm2a
Kdm2b
Kdm4a
Kdm4b
Kdm4c
-2 -1 0 1 2
expression (log2)
B
8mer
mmu-miR-155-5p 3' UGGGGAUAGUGUUAAUCGUAAUU...
Kdm2a 3' UTR
Mouse 5' ...UUUAAAUUAAAUGUAAGCAUUAA...
Human ...UUUAAAUUAAAUGUAAGCAUUAA...
Chimp ...UUUAAAUUAAAUGUAAGCAUUAA...
Rhesus ...UUUAAAUUAAAUGUAAGCAUUAA...
Rat ...UUUAAAUUAAAUGUAAGCAUUAA...
C
IgD MYC KDM2A
GC
50 µm
IgD MYC KDM2A
MYC
KDM2A
D
Co-expression per cell
(KDM2A and MYC)
WT
KO
KDM2A (A.U)
MYC (A.U)
r = 0.775 - 0.788
r = 0.720 - 0.740
E
cMyc- LZ
cMyc+ LZ
cMyc+ DZ
cMyc- DZ
KDM2A MFI in GC-B cells
KDM2A MFI
(relative to nonGC-B)
WT
KO
cMyc+ LZ
low affinity
High affinity
ns
***
KDM2A (relative to non-GCB)
WT low affinity
WT high affinity
KO low affinity
KO high affinity
RCN
KDM2A
F
KDM2A MFI in GC-B cells, High affinity vs. Low affinity
high affinity
Low affinity
HEL3x binding
Igκ
cMyc- LZ
cMyc+ LZ
cMyc+ DZ
cMyc- DZ
High affinity
Low affinity
KDM2A MFI
(relative to nonGC-B)
ns
**
WT
KO

Fig.4

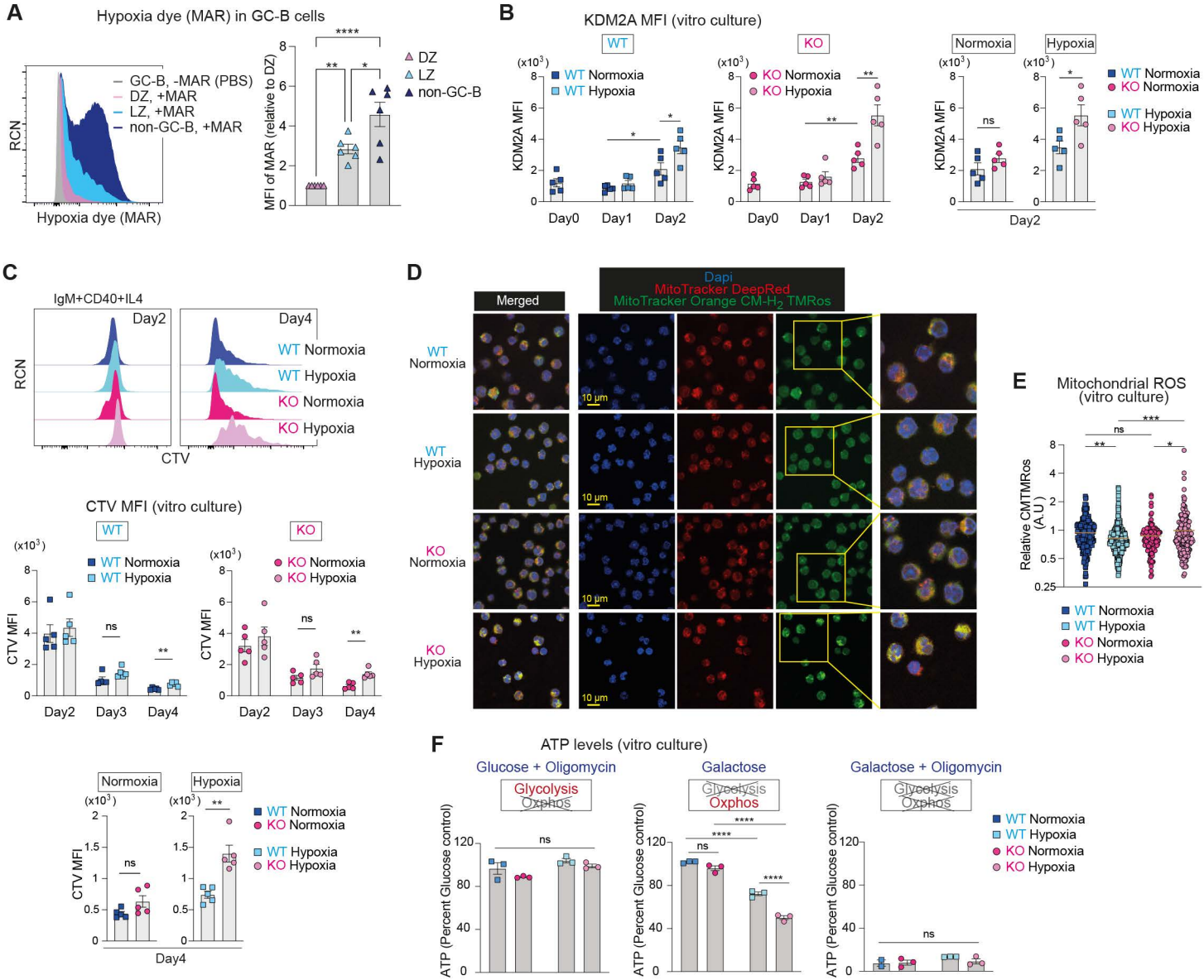
A
Hypoxia dye (MAR) in GC-B cells
GC-B, -MAR (PBS)
DZ, +MAR
LZ, +MAR
non-GC-B, +MAR
RCN
Hypoxia dye (MAR)
MFI of MAR (relative to DZ)
DZ
LZ
non-GC-B
B
KDM2A MFI (vitro culture)
WT
KO
Normoxia
Hypoxia
WT Normoxia
WT Hypoxia
KO Normoxia
KO Hypoxia
KDM2A MFI
Day0
Day1
Day2
C
IgM+CD40+IL4
Day2
Day4
WT Normoxia
WT Hypoxia
KO Normoxia
KO Hypoxia
RCN
CTV
CTV MFI (vitro culture)
CTV MFI
Day2
Day3
Day4
D
Merged
Dapi
MitoTracker DeepRed
MitoTracker Orange CM-H2 TMRos
WT Normoxia
WT Hypoxia
KO Normoxia
KO Hypoxia
10 μm
E
Mitochondrial ROS (vitro culture)
Relative CMTMRos (A.U)
F
ATP levels (vitro culture)
Glucose + Oligomycin
Galactose
Galactose + Oligomycin
Glycolysis
Oxphos
ATP (Percent Glucose control)

Fig.5

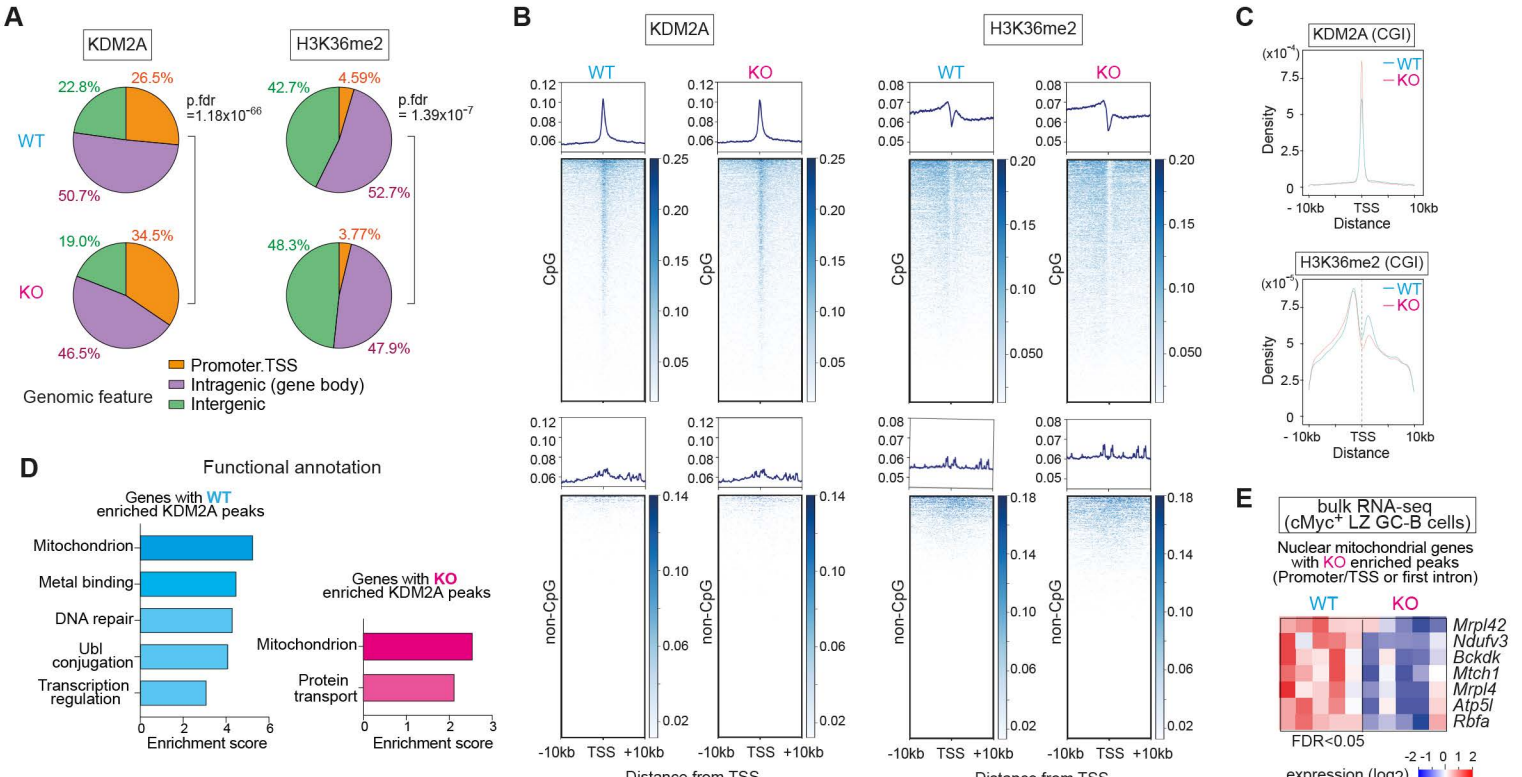
A
KDM2A
H3K36me2
WT
KO
22.8%
26.5%
50.7%
p.fdr =1.18x10^-66
42.7%
4.59%
52.7%
p.fdr = 1.39x10^-7
19.0%
34.5%
46.5%
48.3%
3.77%
47.9%
Genomic feature
Promoter.TSS
Intragenic (gene body)
Intergenic
B
KDM2A
H3K36me2
WT
KO
CpG
non-CpG
-10kb TSS +10kb
Distance from TSS
C
KDM2A (CGI)
H3K36me2 (CGI)
Density
Distance
- 10kb TSS 10kb
D
Functional annotation
Genes with WT enriched KDM2A peaks
Mitochondrion
Metal binding
DNA repair
Ubl conjugation
Transcription regulation
Enrichment score
Genes with KO enriched KDM2A peaks
Mitochondrion
Protein transport
Enrichment score
E
bulk RNA-seq (cMyc+ LZ GC-B cells)
Nuclear mitochondrial genes with KO enriched peaks (Promoter/TSS or first intron)
WT
KO
Mrpl42
Ndufv3
Bckdk
Mtch1
Mrpl4
Atp5l
Rbfa
FDR<0.05
expression (log2)

Fig.6

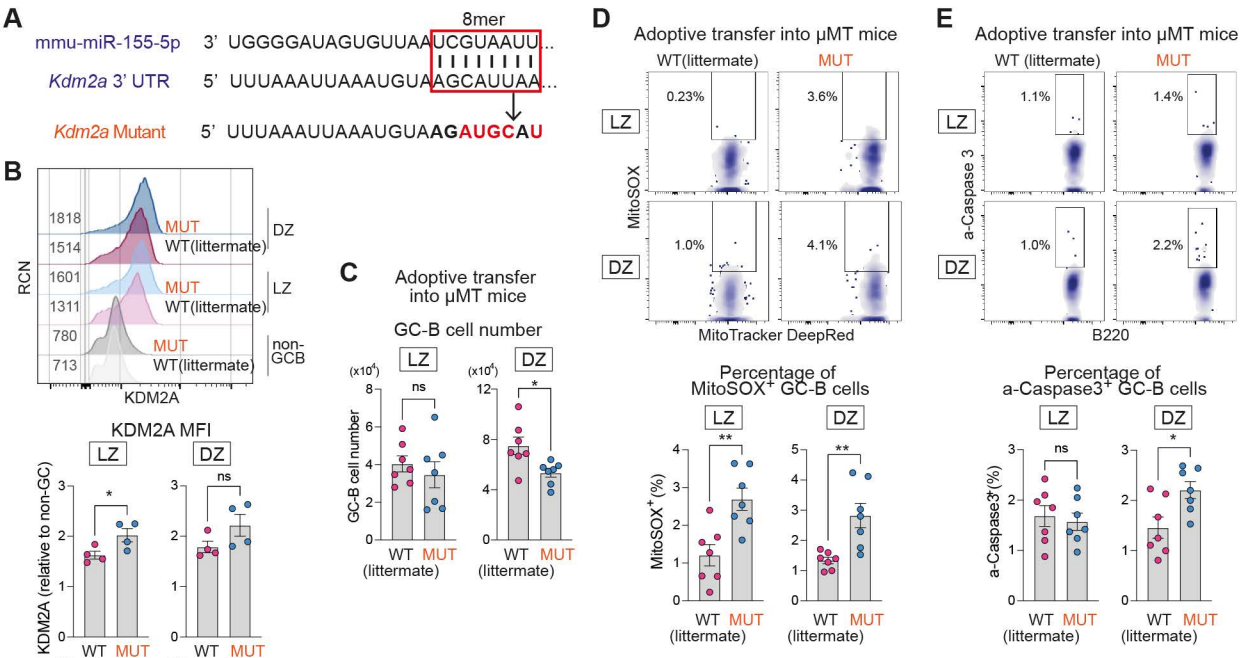
A
8mer
mmu-miR-155-5p 3' UGGGGAUAGUGUUAAUCGUAAUU...
Kdm2a 3' UTR 5' UUUAAAUUAAAUGUAAGCAUUAA...
Kdm2a Mutant 5' UUUAAAUUAAAUGUAAGAUGCAU
B
RCN
1818
1514
1601
1311
780
713
MUT
WT(littermate)
DZ
LZ
non-GCB
KDM2A
KDM2A MFI
LZ
DZ
KDM2A (relative to non-GC)
*
ns
WT (littermate)
MUT
C
Adoptive transfer into μMT mice
GC-B cell number
(x10⁴)
GC-B cell number
ns
*
D
Adoptive transfer into μMT mice
WT(littermate)
MUT
0.23%
3.6%
1.0%
4.1%
MitoSOX
MitoTracker DeepRed
Percentage of MitoSOX⁺ GC-B cells
MitoSOX⁺ (%)
**
E
Adoptive transfer into μMT mice
WT (littermate)
1.1%
1.4%
1.0%
2.2%
a-Caspase 3
B220
Percentage of a-Caspase3⁺ GC-B cells
a-Caspase3⁺(%)

Fig.7

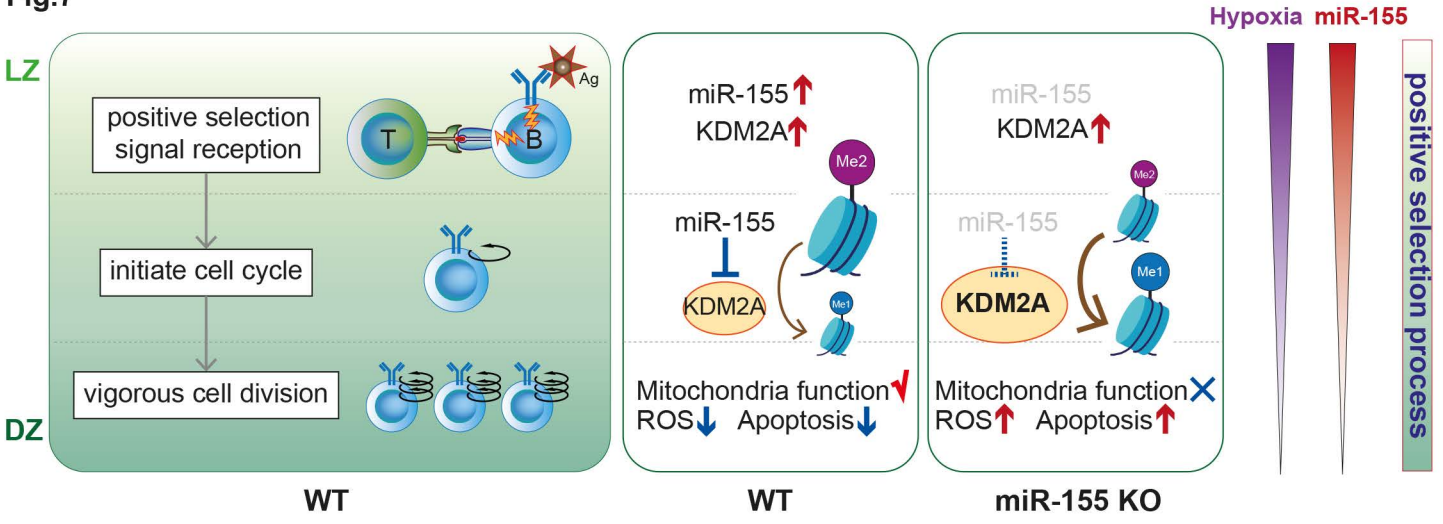
Hypoxia
miR-155
LZ
DZ
positive selection signal reception
initiate cell cycle
vigorous cell division
T
B
Ag
miR-155
KDM2A
Me2
Me1
Mitochondria function
ROS
Apoptosis
positive selection process
WT
WT
miR-155 KO

Supplemental Figure 1 (corresponding to Figure 1).

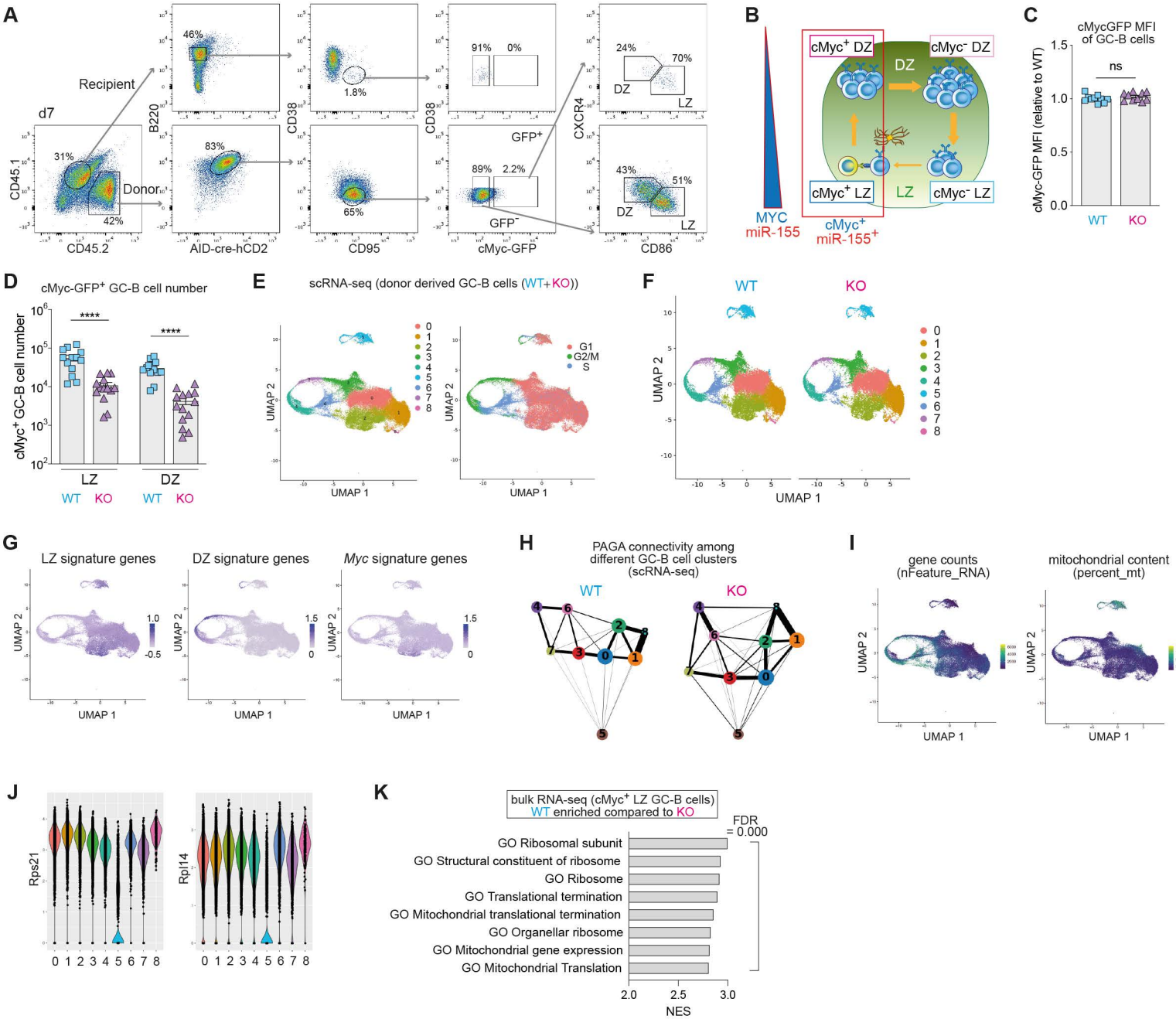

Supplementary Figure 2 (corresponding to Figure 2).

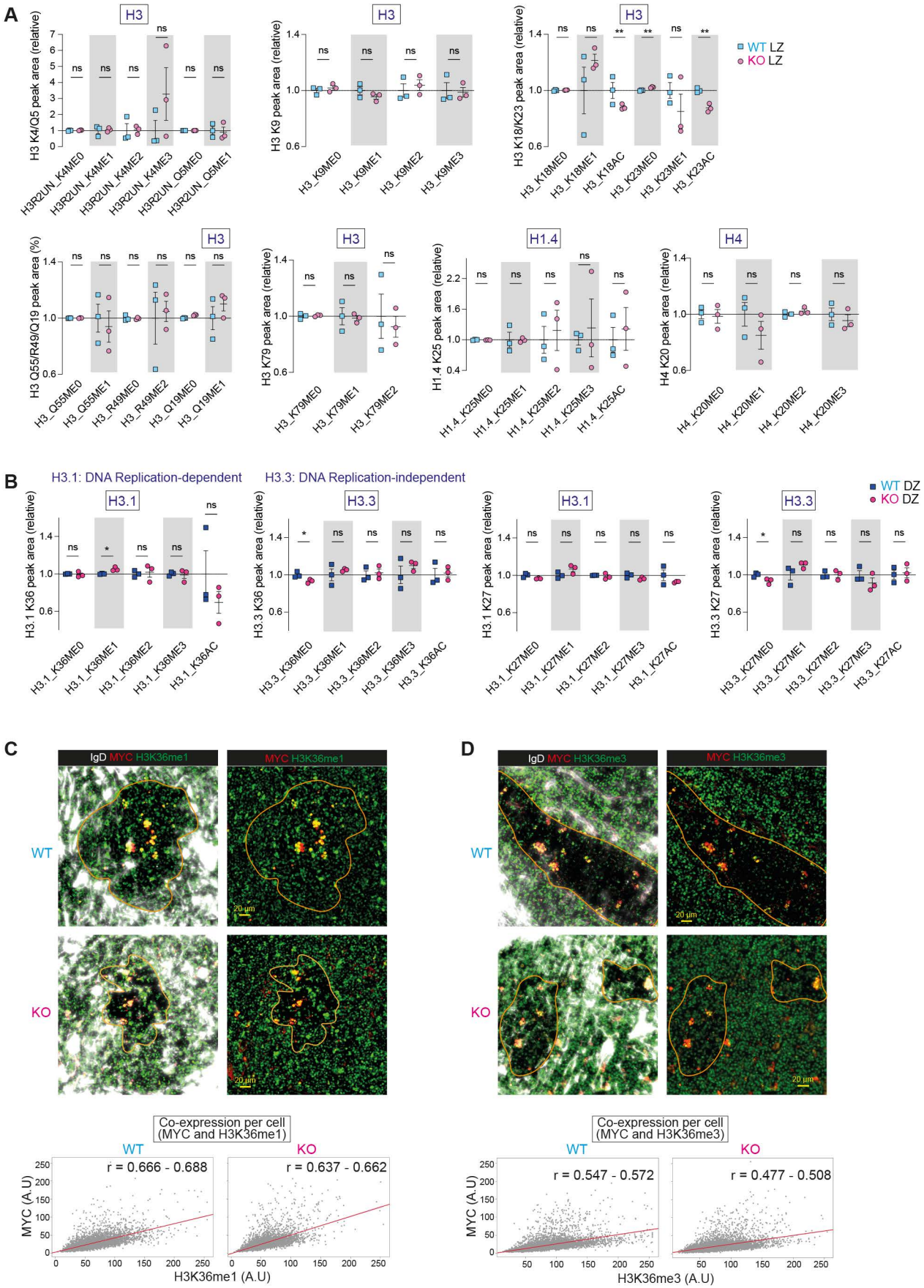

Supplementary Figure 3 (corresponding to Figure 3).

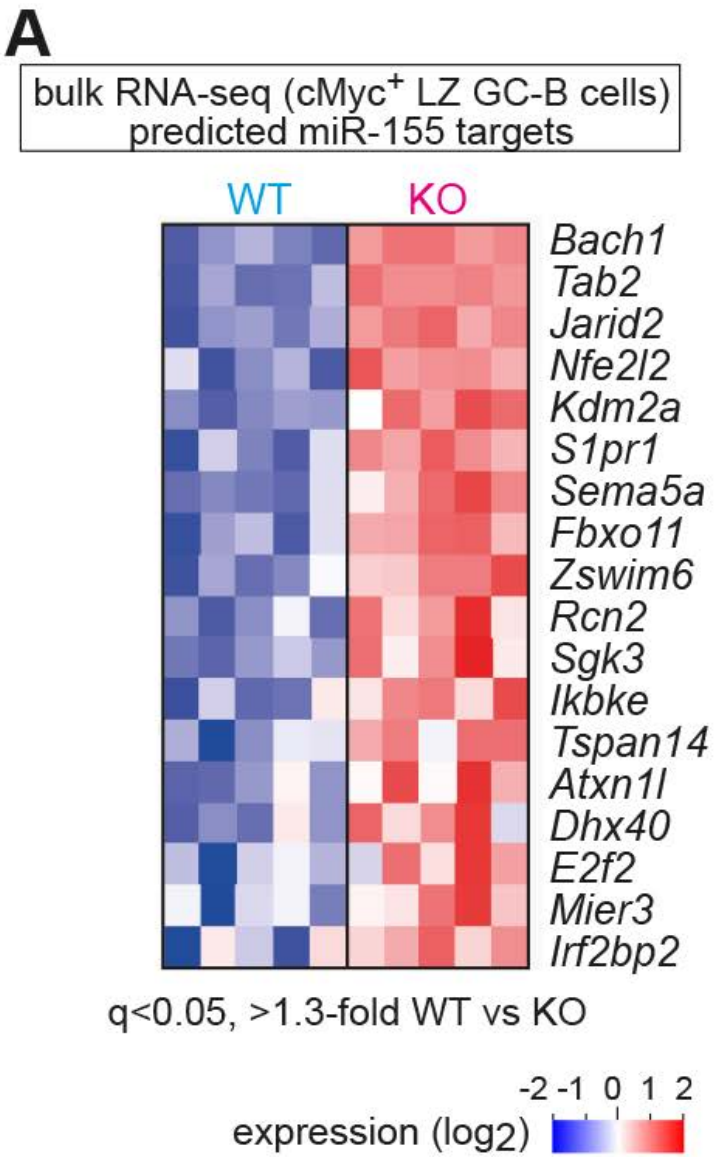

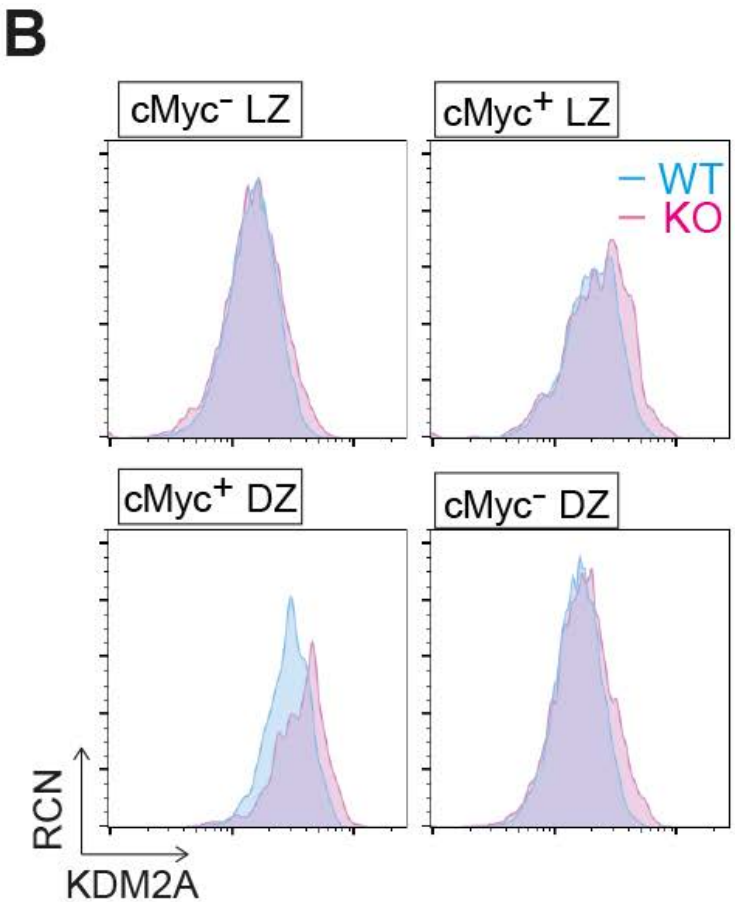

Supplementary Figure 4 (corresponding to Figure 4).

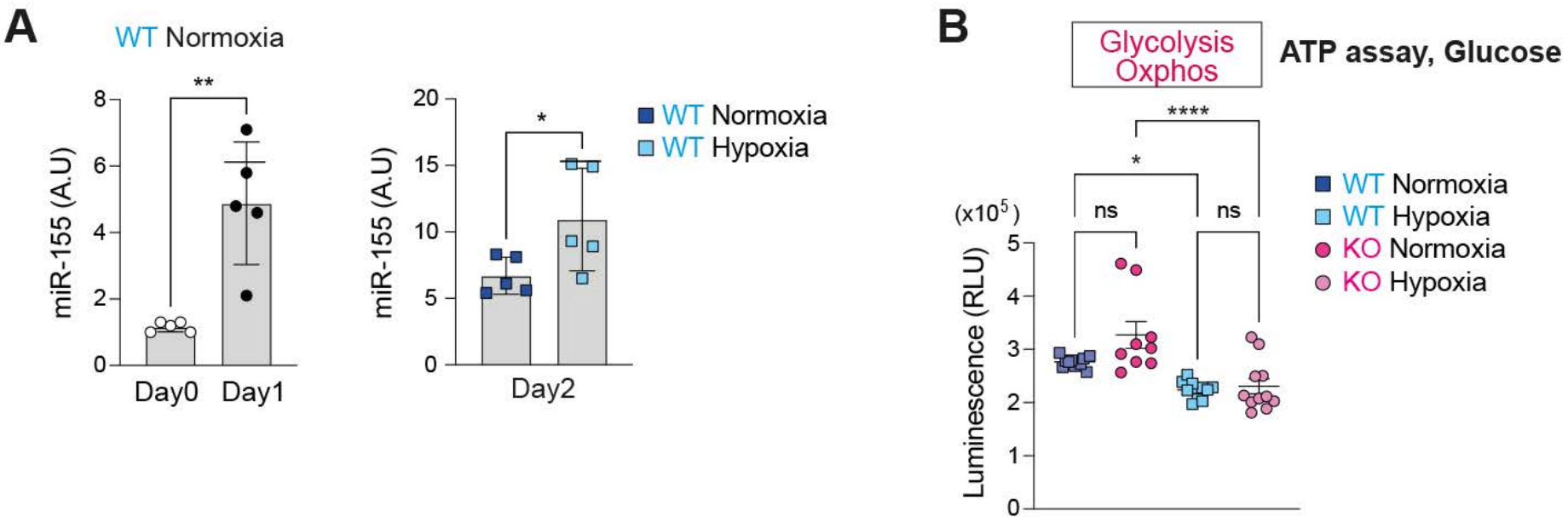
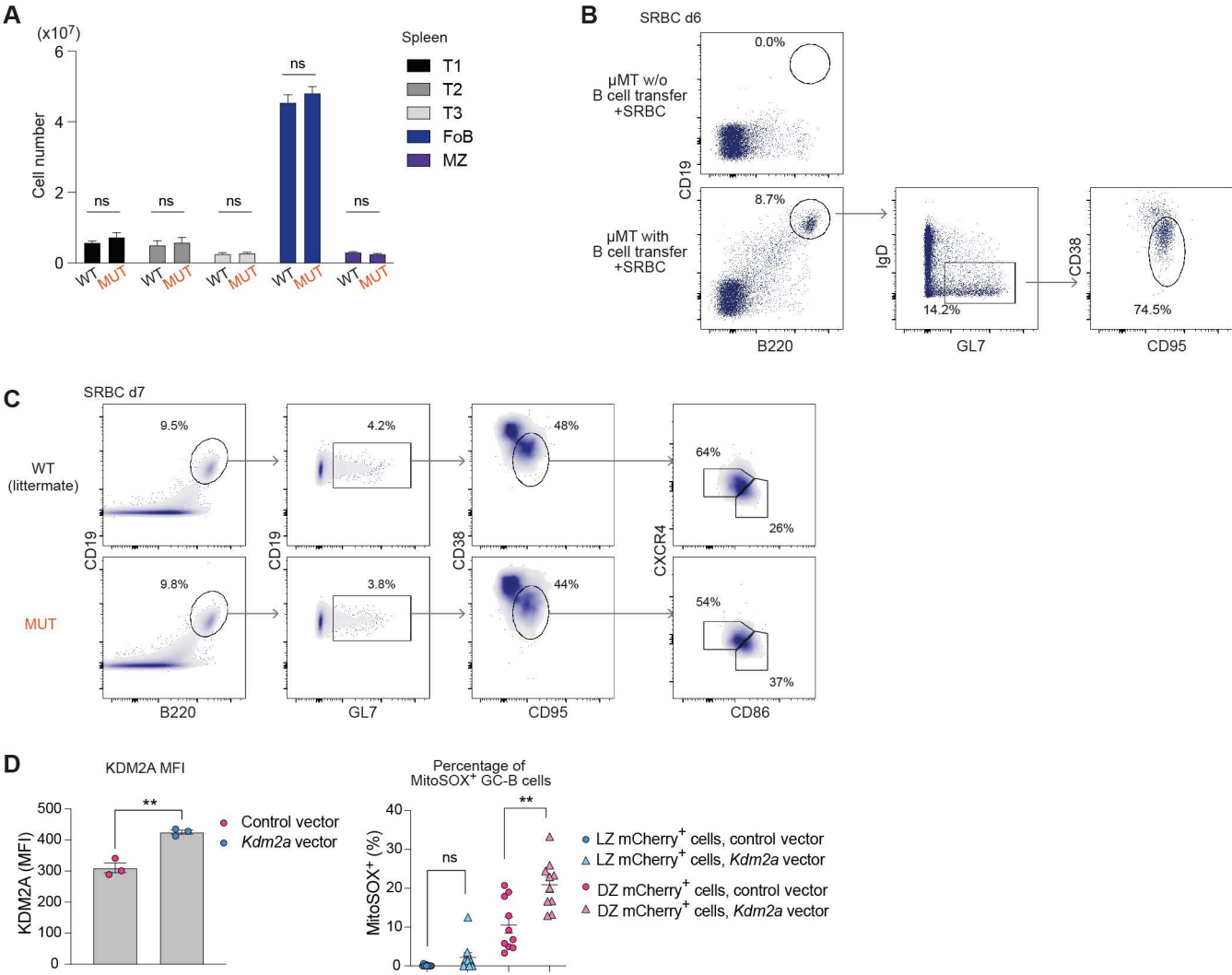
Supplementary Figure 5 (corresponding to Figure 6).